Multimodal state-dependent connectivity analysis of arousal and autonomic centers in the brainstem and basal forebrain

Haatef Pourmotabbed[a, b, c], Caroline G. Martin[b, c, d], Sarah E. Goodale[a, b, c], Derek J. Doss[a, b, c], Shiyu Wang[a, b, c], Roza G. Bayrak[b, c, d], Hakmook Kang[e], Victoria L. Morgan[a, b, c, f, g], Dario J. Englot[a, b, c, d, f, g], Catie Chang[a, b, c, d]

Affiliations:

[a]Department of Biomedical Engineering, Vanderbilt University, Nashville, TN, USA

[b]Vanderbilt University Institute of Imaging Science, Vanderbilt University Medical Center, Nashville, TN, USA

[c]Vanderbilt Institute for Surgery and Engineering, Vanderbilt University, Nashville, TN, USA

[d]Department of Electrical and Computer Engineering, Vanderbilt University, Nashville, TN, USA

[e]Department of Biostatistics, Vanderbilt University, Nashville, TN, USA

[f]Department of Radiology and Radiological Sciences, Vanderbilt University Medical Center, Nashville, TN, USA

[g]Department of Neurological Surgery, Vanderbilt University Medical Center, Nashville, TN, USA

Corresponding author:

Haatef Pourmotabbed
Department of Biomedical Engineering
Vanderbilt University, Nashville, TN, USA
haatef.pourmotabbed@vanderbilt.edu

ABSTRACT

Vigilance is a continuously altering state of cortical activation that influences cognition and behavior and is disrupted in multiple brain pathologies. Neuromodulatory nuclei in the brainstem and basal forebrain are implicated in arousal regulation and are key drivers of widespread neuronal activity and communication. However, it is unclear how their large-scale brain network architecture changes across dynamic variations in vigilance state (i.e., alertness and drowsiness). In this study, we leverage simultaneous EEG and 3T multi-echo functional magnetic resonance imaging (fMRI) to elucidate the vigilance-dependent connectivity of arousal regulation centers in the brainstem and basal forebrain. During states of low vigilance, most of the neuromodulatory nuclei investigated here exhibit a stronger global correlation pattern and greater connectivity to the thalamus, precuneus, and sensory and motor cortices. In a more alert state, the nuclei exhibit the strongest connectivity to the salience, default mode, and auditory networks. These vigilance-dependent correlation patterns persist even after applying multiple preprocessing strategies to reduce systemic vascular effects. To validate our findings, we analyze two large 3T and 7T fMRI datasets from the Human Connectome Project and demonstrate that the static and vigilance-dependent connectivity profiles of the arousal nuclei are reproducible across 3T multi-echo, 3T single-echo, and 7T single-echo fMRI modalities. Overall, this work provides novel insights into the role of neuromodulatory systems in vigilance-related brain activity.

1. INTRODUCTION

Vigilance is a continuously altering state of physiological and psychological activation (i.e., alertness and drowsiness) that impacts the ability of the brain to process information and respond to external stimuli (Oken et al., 2006; Sara and Bouret, 2012). Higher levels of alertness result in enhanced cognitive processing, greater emotional reactivity, and an improved capability for sustained attention (Canales-Johnson et al., 2020; Franzen et al., 2008; Jagannathan et al., 2022). Additionally, impairments of vigilance occur in multiple brain pathologies and contribute to the development of neurocognitive deficits in executive function and attention. These vigilance impairments include hyperarousal in neuropsychiatric disorders (Hegerl and Hensch, 2014; Xie et al., 2024) and excessive daytime sleepiness and sleep-wake disturbances in traumatic brain injury, epilepsy, Alzheimer's disease, and Parkinson's disease (Englot et al., 2020; Rothman and Mattson, 2012; Sandsmark et al., 2017). Identifying the neural circuit mechanisms underlying alterations in vigilance state may aid in uncovering novel therapies for neurocognitive deficits in various brain disorders.

Key drivers of widespread neuronal activity and communication include neuromodulatory centers in the brainstem and basal forebrain (van den Brink et al., 2019). These neuromodulatory nuclei consist of monoaminergic, glutamatergic, and cholinergic neurons that project to the thalamus, hypothalamus, and widespread areas of the cortex, mediating cortical activation and autonomic function (Brown et al., 2012; Edlow et al., 2012; Scammell et al., 2017; Zaborszky et al., 2008). Human and animal studies have provided evidence that the neuronal activity of neuromodulatory nuclei is associated with changes in widespread cortical activity, brain network organization, and markers of arousal and attention (Grimm et al., 2024; Liu et al., 2018; Taylor et al., 2022; Zerbi et al., 2019). For instance, blood oxygenation level dependent (BOLD) signals in the locus coeruleus (LC) and nucleus basalis of Meynert (NBM) have been shown to be correlated with pupil diameter, low-frequency electrophysiological activity, and attentional task response (Joshi et al., 2016; Liu et al., 2018; Murphy et al., 2014). Furthermore, pharmacological studies have found that inactivation of neurons in the NBM leads to suppression of global brain signals (Turchi et al., 2018) and modulation of monoamine neurotransmitters results in altered resting-state functional connectivity (FC) (van den Brink et al., 2016).

Neuroimaging studies in healthy individuals have sought to characterize the structural and functional connectivity of neuromodulatory nuclei in the brainstem and basal forebrain (Bar et al., 2016; Beliveau et al., 2015; Cauzzo et al., 2022; Hansen et al., 2024; Yuan et al., 2019; Zhang et al., 2016). Abnormalities in the connectivity of these subcortical regions have also been observed in multiple neurological conditions, suggesting that mapping of the FC may provide a valuable avenue for identifying brain targets for therapeutic neuromodulation (Edlow et al., 2021; Englot et al., 2020; Gonzalez et al., 2021; Kelberman et al., 2020; Serra et al., 2018). However, to date, functional magnetic resonance imaging (fMRI) studies have not comprehensively mapped vigilance-related alterations in the FC of the brainstem and basal forebrain. Dynamic changes in the spatiotemporal activity and FC of the cortex have been linked to altering states of alertness and wakefulness (Liu and Falahpour, 2020; Martin et al., 2021). These state-dependent effects are often unaccounted for due to the difficulty in estimating vigilance based on fMRI alone (Goodale et al., 2021; Liu and Falahpour, 2020; Martin et al.,

44 2021). Subcortical neuromodulatory systems may be involved in coordinating arousal changes
45 in the cortex (Brown et al., 2012; Scammell et al., 2017), and characterizing the vigilance-
46 dependent connectivity of the subcortical activating structures can provide novel insights into
47 their role in regulating brain activity. Therefore, in this study, we leveraged simultaneously
48 recorded electroencephalography (EEG) and fMRI data to elucidate the functional network
49 architecture of neuromodulatory nuclei in different vigilance states. The EEG data were used to
50 identify time periods of alertness and drowsiness (Olbrich et al., 2009; Sander et al., 2015), and
51 the whole-brain correlation patterns of nine brainstem and two bilateral basal forebrain regions
52 of the ascending arousal network were compared between the two vigilance states (Edlow et
53 al., 2024; Edlow et al., 2012; Zaborszky et al., 2008).

54 In addition to the vigilance-dependent FC analysis, we evaluated the ability of fMRI to reliably
55 characterize the FC of nuclei in the brainstem and basal forebrain. Functional MRI
56 investigations of brainstem and basal forebrain nuclei are challenging because of their small
57 size, heterogeneity in location across individuals, and susceptibility to contamination by
58 physiological noise due to their close proximity to major blood vessels, subarachnoid cisterns,
59 and the ventricles (Beissner, 2015; Brooks et al., 2013). Advanced acquisition techniques, such
60 as multi-echo sequences and 7T fMRI, may alleviate some of these limitations by improving the
61 BOLD contrast, signal-to-noise ratio (SNR), and spatial resolution and specificity (Chang et al.,
62 2016; Sclocco et al., 2018; Turker et al., 2021). In particular, multi-echo independent component
63 analysis can remove non-BOLD artifacts caused by head motion and cyclic physiological noise
64 (Kundu et al., 2013; Kundu et al., 2012). Additional preprocessing methods that estimate and
65 regress out non-neuronal BOLD signals originating from systemic vascular effects may also
66 improve the SNR (Brooks et al., 2013; Caballero-Gaudes and Reynolds, 2017).

67 We implemented a 3T multi-echo fMRI paradigm for the simultaneous EEG-fMRI dataset to
68 mitigate SNR limitations caused by non-BOLD motion and physiological noise, and we used two
69 large datasets of 3T and 7T single-echo fMRI from the Human Connectome Project (Smith et
70 al., 2013) to quantify the spatial reproducibility of the static whole-brain correlation patterns of
71 the neuromodulatory nuclei across different field strengths and acquisition methods. Because
72 the optimal preprocessing strategy for analysis of subcortical fMRI remains an open question
73 (Beissner, 2015; Sclocco et al., 2018; Turker et al., 2021), the FC patterns were also compared
74 between three preprocessing pipelines designed to remove non-neuronal influences. Finally, we
75 analyzed simultaneous fMRI and pupillometry recordings in the HCP 7T dataset to assess the
76 reproducibility of the vigilance-dependent FC profiles of the subcortical nuclei between the EEG-
77 fMRI and HCP 7T datasets.

78 **2. RESULTS**

79 This study included resting-state fMRI data from three datasets (see **Table 1** for a detailed
80 description of each dataset). The first dataset consisted of simultaneous EEG and 3T multi-echo
81 fMRI data collected at Vanderbilt University (VU 3T-ME dataset: n = 30 healthy subjects). The
82 other two datasets consisted of 3T and 7T single-echo, multi-band fMRI from a large number of
83 subjects in the HCP database (HCP 3T dataset: n = 375; HCP 7T dataset: n = 176) (Smith et
84 al., 2013). Non-BOLD physiological and motion artifacts in the fMRI data were removed with
85 multi-echo independent component analysis (ME-ICA) in the VU 3T-ME dataset (Kundu et al.,

3

86 2013; Kundu et al., 2012; Turker et al., 2021) and with ICA-FIX in the HCP 3T and 7T datasets
87 (Smith et al., 2013). fMRI signals were extracted from subcortical regions-of-interest (ROIs)
88 involved in arousal and autonomic regulation (hereafter referred to as "arousal ROIs"). The
89 arousal ROIs consist of monoaminergic, glutamatergic, and cholinergic nuclei in the brainstem
90 (9 ROIs) (Edlow et al., 2024; Edlow et al., 2012) and basal forebrain (2 bilateral ROIs)
91 (Zaborszky et al., 2008) (see **Table 2**).

92 **Table 1.** Demographic and technical information for the three datasets used in this study: simultaneous
93 EEG and 3T multi-echo fMRI from Vanderbilt University (VU) and 3T and 7T single-echo fMRI from the
94 Human Connectome Project (HCP S1200 data release).

Dataset	VU 3T-ME	HCP 3T	HCP 7T
Number of Subjects (n)	30	375	176
Number of Sessions (n)	45 (1-2 per subject)	1500 (4 per subject)	704 (4 per subject)
Age (mean ± SD years)	35.1 ± 15.3	28.5 ± 3.8	29.4 ± 3.3
Gender (M/F)	14/16	207/168	70/106
fMRI Modality	3T multi-echo fMRI	3T single-echo fMRI	7T single-echo fMRI
Scalp EEG	Yes (30 subjects)	No	No
Respiratory belt and PPG	Yes (28 subjects)	Yes (375 subjects)	No
Pupillometry	No	No	Yes (145 subjects)

95

96 **Table 2.** Seed regions-of-interest (ROIs) used for the whole-brain connectivity analysis. The ROIs are
97 involved in arousal and autonomic regulation and consist of monoaminergic, glutamatergic, and
98 cholinergic nuclei in the brainstem (Harvard Ascending Arousal Network [AAN] atlas Version 1.0;
99 https://www.nmr.mgh.harvard.edu/resources/aan-atlas) (Edlow et al., 2024; Edlow et al., 2012) and basal
100 forebrain (JuBrain Anatomy Toolbox; https://www.fz-juelich.de/en/inm/inm-7/resources/jubrain-anatomy-
101 toolbox) (Zaborszky et al., 2008).

Brain Area	Region-of-interest (ROI)	Main neurotransmitter systems (Brown et al., 2012; Edlow et al., 2012; Scammell et al., 2017)
Brainstem	Locus coeruleus (LC)	Norepinephrine
Brainstem	Dorsal raphe (DR)	Serotonin
Brainstem	Median raphe (MR)	Serotonin
Brainstem	Ventral tegmental area (VTA)	Dopamine
Brainstem	Periaqueductal gray (PAG)	Dopamine, GABA
Brainstem	Parabrachial nuclear complex (PBC)	Glutamate
Brainstem	Cuneiform/subcuneiform nucleus (CSC)	Glutamate, GABA
Brainstem	Pedunculopontine nucleus (PPN)	Acetylcholine, glutamate, GABA
Brainstem	Nucleus pontine oralis (PO)	Acetylcholine, glutamate, GABA
Basal Forebrain	Nucleus basalis of Meynert (NBM)	Acetylcholine, glutamate, GABA
Basal Forebrain	Medial septum/diagonal band of Broca (MS/DBB)	Acetylcholine, glutamate, GABA

102

103 The quality of the fMRI signals of the arousal ROIs was assessed by computing the temporal
104 SNR (tSNR) (shown in **Supplementary Fig. 1**) from the ME-ICA denoised data in the VU 3T-
105 ME dataset and from the ICA-FIX denoised data in the HCP datasets. The tSNR of the arousal
106 ROIs was greater for the VU 3T-ME dataset compared to the HCP 3T and 7T datasets. In the
107 VU 3T-ME dataset, the tSNR of the arousal ROIs was comparable to the tSNR of cortical ROIs
108 from the Schaefer atlas (Schaefer et al., 2018). In the HCP 3T and 7T datasets, the tSNR of the
109 arousal ROIs was lower than that of the cortical ROIs.

4

2.1. Cross-modality reproducibility of static connectivity patterns

The whole-brain static FC patterns of the arousal ROIs were estimated by computing the seed-based correlation over the entire fMRI scan duration. The seed-based correlation was calculated after removal of mean white matter (WM), deep cerebrospinal fluid (CSF), and fourth ventricle (FV) signals from the fMRI data (i.e., the mCSF/WM pipeline). The mCSF/WM pipeline is described in more detail in the **Methods** section and was performed to mitigate non-neural influences due to systemic vascular effects (Caballero-Gaudes and Reynolds, 2017; Turker et al., 2021). FC t-maps were then computed for the group average of the seed-based correlation patterns in each dataset, and the t-maps were thresholded to portray the strongest significant correlations (threshold of $p_{FDR} < 0.05$ and 40% of the top t-values). The static FC t-maps of the LC, cuneiform/subcuneiform nucleus (CSC), and NBM are depicted in **Fig. 1a**, and the static FC t-maps of all the arousal ROIs are provided in a Neurovault repository (available upon acceptance of this manuscript; NIFTI file format). For ease of visualization, the spatial overlap of the static FC t-maps with 16 canonical brain network templates from the FINDLAB and Melbourne atlases (Shirer et al., 2012; Tian et al., 2020) was also computed (see **Fig. 1b**).

Fig. 1

The Dice similarity coefficient (DSC) was used to evaluate the reproducibility of the thresholded static FC t-maps across the three fMRI modalities (see **Fig. 1c**) (Turker et al., 2021). We found that the reproducibility across all three modalities was moderate to good for all of the arousal ROIs (DSC = 0.59-0.68 [interquartile range; IQR]), except for the periaqueductal gray (PAG) between the HCP 3T and 7T datasets. The FC pattern of the ventral tegmental area (VTA) had the lowest reproducibility between the VU 3T-ME and HCP 3T datasets while the FC of the PAG and medial septum/diagonal band of Broca (MS/DBB) had the lowest reproducibility between the VU 3T-ME and HCP 7T datasets. The FC of the PAG also had the lowest reproducibility between the HCP 3T and 7T datasets.

In agreement with the moderate to good reproducibility, the thresholded FC patterns of most of the arousal ROIs were qualitatively similar between the three fMRI modalities. The LC exhibited strong positive correlations to regions of the thalamus, precuneus, basal ganglia, and salience, default mode, sensorimotor, and visual networks. The FC patterns of the other brainstem ROIs were relatively similar to that of the LC (see **Supplementary Fig. 2** for the spatial similarity of the FC patterns between the arousal ROIs). The NBM exhibited strong positive correlations to regions of the thalamus, basal ganglia, mesial temporal lobe, and salience, default mode, auditory, language, and sensorimotor networks. Notable differences between the fMRI modalities include less spatial overlap of the FC patterns of the brainstem ROIs with the sensorimotor cortex in the HCP 3T dataset and greater spatial overlap with the executive control network and higher-order visual cortex in the HCP 3T and 7T datasets.

2.2. EEG-based vigilance-dependent connectivity patterns

We leveraged simultaneous EEG and fMRI data in the VU 3T-ME dataset to derive vigilance-dependent FC patterns for the arousal ROIs. Time periods of alert and drowsy vigilance states were identified from the EEG data using an adapted version of the Vigilance Algorithm Leipzig (VIGALL) algorithm (see **Fig. 2a** for an illustration of the vigilance staging algorithm) (Huang et

151 al., 2015; Jawinski et al., 2019; Sander et al., 2015). Whole-brain FC t-maps were then
152 computed for the group average of the seed-based correlation patterns of the arousal ROIs in
153 each state separately and for the effect of vigilance state (drowsy versus alert) on the
154 correlation patterns. The alert, drowsy, and drowsy versus alert FC t-maps were thresholded to
155 portray the strongest significant correlations (threshold of $p_{FDR} < 0.05$ and 40% of the top t-
156 values). The vigilance-dependent FC t-maps of the LC, CSC, and NBM are depicted in **Fig. 2b**,
157 and the vigilance-dependent FC t-maps of all the arousal ROIs are provided in the Neurovault
158 repository. The spatial overlap of the FC t-maps with the canonical brain network templates is
159 shown in **Fig. 2c**.

160 <div align="center">**Fig. 2**</div>

161 We found that the FC of all the arousal ROIs, except for the dorsal raphe (DR) and MS/DBB,
162 were significantly different between the alert and drowsy states. The LC, CSC, median raphe
163 (MR), parabrachial nuclear complex (PBC), nucleus pontine oralis (PO), and NBM had the
164 greatest vigilance-related FC alterations. In general, the arousal ROIs exhibited a stronger
165 global correlation pattern in the drowsy compared to the alert state. The brainstem ROIs had the
166 strongest drowsy versus alert FC differences in regions of the thalamus, precuneus, and
167 salience, ventral default mode, sensorimotor, auditory, and visual networks while the NBM had
168 the strongest drowsy versus alert FC differences in regions of the mesial temporal lobe and
169 executive control, salience, ventral default mode, language, sensorimotor, auditory, and higher-
170 order visual networks.

171 In the separate alert and drowsy states, the thresholded FC patterns of the arousal ROIs had
172 similar spatial profiles as their static FC patterns. Most of the arousal ROIs had strong positive
173 correlations to the thalamus, precuneus, and salience, default mode, auditory, and sensorimotor
174 networks in both the alert and drowsy states. The ROIs also had strong correlations to the visual
175 networks in the drowsy state. The FC patterns of most of the ROIs in the alert state had more
176 spatial overlap with the dorsal default mode network than the FC patterns in the drowsy state
177 while the FC in the drowsy state had more spatial overlap with the visual networks. The FC of
178 most of the ROIs in both the alert and drowsy states had more spatial overlap with the auditory
179 network compared to their static FC patterns.

180 **2.3. Cross-modality reproducibility of vigilance-dependent connectivity patterns**

181 We evaluated the cross-modality reproducibility of the state-dependent FC patterns of the
182 arousal ROIs that had the greatest vigilance-related FC alterations in the VU 3T-ME dataset
183 (i.e., LC, CSC, MR, PBC, PO, and NBM). An unsupervised clustering algorithm was used to
184 derive dynamic FC states in the VU 3T-ME and HCP 7T datasets, and markers of vigilance
185 were estimated from the simultaneous EEG data in the VU 3T-ME dataset and from the
186 simultaneous pupillometry recordings in the HCP 7T dataset. The unsupervised clustering was
187 performed by first computing the dynamic FC of the arousal ROIs with sliding window
188 correlations. The k-means algorithm was then employed to spatially cluster the dynamic FC
189 patterns of each ROI into two states (Wang et al., 2016). Whole-brain FC t-maps were derived
190 for the group average of the sliding window correlation patterns in each state separately and for
191 the effect of state (state 2 versus state 1) on the correlation patterns. The FC t-maps were

192 thresholded at p_{FDR} < 0.05 and at 40% of the top t-values, and the DSC was used to evaluate
193 the reproducibility of the single- and two-state FC t-maps between the VU 3T-ME and HCP 7T
194 datasets. The state-dependent FC t-maps of the LC and NBM are depicted in **Fig. 3a-b**, and the
195 FC t-maps of all the arousal ROIs (i.e., LC, CSC, MR, PBC, PO, and NBM) are provided in the
196 Neurovault repository.

197   **Fig. 3**

198 In the VU 3T-ME dataset, the VIGALL-based alert/drowsy staging algorithm was used to assign
199 a vigilance score to each time window based on the EEG data. In the HCP 7T dataset, the
200 percent duration of eye closure was computed from the pupillometry recordings and used as a
201 putative marker of vigilance (Abe, 2023; Shekari Soleimanloo et al., 2019; Soon et al., 2021;
202 Wang et al., 2016). We found that, for each arousal ROI, the VIGALL score was significantly
203 lower and the percent eye closure was significantly greater for state 2 compared to state 1 (p_{FDR}
204 < 0.05; see **Fig. 3c**), suggesting that state 2 primarily corresponds to a state of drowsiness. The
205 VIGALL scores of the time windows in state 1 were evenly distributed between alert and drowsy
206 classifications (46-47% [IQR] percent alert and 47-49% [IQR] percent drowsy), suggesting that
207 state 1 corresponds to a mixed state of alertness and drowsiness. The time windows in state 2
208 were primarily classified as drowsy (6-9% [IQR] percent alert and 81-87% [IQR] percent
209 drowsy).

210 The single- and two-state FC t-maps had a high cross-modality reproducibility for the LC, CSC,
211 MR, PBC, PO, and NBM (DSC = 0.62-0.68 [IQR]; see **Fig. 3d**), and the FC patterns were
212 qualitatively similar between the VU 3T-ME and HCP 7T datasets. Similar to the EEG-derived
213 drowsy versus alert FC patterns in the VU 3T-ME dataset, the FC of the arousal ROIs exhibited
214 a stronger global correlation pattern in state 2 compared to state 1, with greater FC to regions of
215 the thalamus, precuneus, and salience, ventral default mode, auditory, sensorimotor, and visual
216 networks. Likewise, the thresholded single-state FC maps exhibited a similar correlation pattern
217 as their EEG-derived alert and drowsy counterparts. The FC patterns in state 1 had more spatial
218 overlap with the dorsal default mode network than the FC patterns in state 2, and the FC in
219 state 2 had more overlap with the auditory, sensorimotor, and visual networks.

220 **2.4. Influence of preprocessing on the static connectivity**

221 In addition to the mCSF/WM pipeline, the fMRI data were preprocessed with two alternative
222 strategies for removing systemic vascular effects (i.e., the physio and aCompCor pipelines)
223 (Caballero-Gaudes and Reynolds, 2017). We then compared the static FC of the arousal ROIs
224 in the VU 3T-ME, HCP 3T, and HCP 7T datasets between the three preprocessing pipelines.
225 The aCompCor pipeline is a more aggressive method of removing signals from the WM and
226 CSF (Behzadi et al., 2007) while the physio pipeline involves confound regression of low-
227 frequency physiological effects associated with heart rate and respiration (Chen et al., 2020).
228 The static FC t-maps of the LC, CSC, and NBM for the physio and aCompCor pipelines are
229 depicted in **Supplementary Fig. 3**.

230 The mCSF/WM and physio pipelines resulted in largely similar static FC patterns for the arousal
231 ROIs, and the cross-modality reproducibility of the static FC was similar for the mCSF/WM and
232 physio pipelines (DSC = 0.59-0.68 [IQR] for the mCSF/WM pipeline and DSC = 0.56-0.62 [IQR]

233 for the physio pipeline; see **Supplementary Fig. 4**). The aCompCor pipeline led to a global

234 decrease in the FC strength in all three fMRI modalities, primarily in the sensory and motor

235 networks, and resulted in significant negative correlations for most of the arousal ROIs in the

236 HCP 3T and 7T datasets. The cross-modality reproducibility was lower for most of the ROIs in

237 the aCompCor pipeline compared to the other pipelines (DSC = 0.44-0.60 [IQR] for the

238 aCompCor pipeline). However, the aCompCor pipeline improved the reproducibility between the

239 HCP 3T and 7T datasets for the PAG, MS/DBB, and NBM.

2.5. Influence of preprocessing on the vigilance-dependent connectivity

241 We also compared the EEG-based vigilance-dependent FC of the arousal ROIs in the VU 3T-

242 ME dataset between the mCSF/WM, physio, and aCompCor pipelines. The vigilance-dependent

243 FC t-maps of the LC, CSC, and NBM for the physio and aCompCor pipelines are depicted in

244 **Supplementary Fig. 5**. Preprocessing the fMRI data through the physio pipeline resulted in less

245 pronounced vigilance-related FC alterations compared to the mCSF/WM pipeline, and only the

246 FC patterns of the CSC, MR, PBC, PO, VTA, and NBM were significantly different between the

247 alert and drowsy states. The CSC, MR, and PBC had the greatest vigilance-related FC

248 alterations, with similar spatial profiles as those in the mCSF/WM pipeline. Likewise, the

249 reproducibility of the drowsy versus alert FC patterns between the mCSF/WM and physio

250 pipelines was moderate to good for the CSC, MR, PBC, and VTA and poor for the PO and NBM

251 (DSC = 0.37-0.61 [IQR]; see **Supplementary Fig. 6**). The reproducibility of the FC maps in the

252 alert and drowsy states between the mCSF/WM and physio pipelines was high for all of the

253 arousal ROIs (DSC = 0.77-0.79 [IQR]), except for the MS/DBB in the alert state.

254 None of the arousal ROIs had significant FC alterations between alert and drowsy states for the

255 aCompCor pipeline, and the overall strength of the FC patterns in the alert and drowsy states

256 was reduced compared to the mCSF/WM and physio pipelines. The reproducibility of the FC

257 maps in the alert and drowsy states between the aCompCor and the other two pipelines was

258 poor to moderate for most of the arousal ROIs (DSC = 0.29-0.51 [IQR]).

3. DISCUSSION

260 Using simultaneous EEG and 3T multi-echo fMRI data, we investigated the whole-brain

261 functional network architecture of arousal regulation centers in the brainstem and basal

262 forebrain across EEG-derived states of vigilance. Our results revealed that the FC of most of the

263 arousal ROIs was dependent on the vigilance level, with a stronger global correlation pattern in

264 the drowsy state compared to the alert state. These state-dependent FC patterns were

265 replicated in an independent 7T single-echo fMRI dataset in which pupillometry was used to

266 assess vigilance. Furthermore, we found that the vigilance-related FC alterations were reduced

267 but not completely removed when regressing out low-frequency physiological effects modeled

268 from respiration and heart rate signals. Finally, we demonstrated that the most dominant

269 connections of the static FC profiles of the brainstem and basal forebrain nuclei were

270 reproducible across 3T multi-echo, 3T single-echo, and 7T single-echo fMRI modalities.

271 Most of the arousal ROIs had a stronger global correlation pattern in the EEG-derived drowsy

272 state compared to the alert state, with stronger FC to the thalamus, precuneus, and sensory and

273 motor networks. Previous studies have shown that the amplitude of global fMRI fluctuations is

274 increased at lower vigilance levels and is dominated by higher signal power in sensory and
275 motor regions (Falahpour et al., 2018; Liu and Falahpour, 2020; Pourmotabbed et al., 2024;
276 Wong et al., 2013). This fMRI signature of vigilance is conserved across multiple experimental
277 conditions (i.e., resting-state, sleep, and sedation) (Li et al., 2023). Likewise, prior work has
278 discovered the existence of propagating global slow waves in fMRI that are associated with
279 arousal transitions and are more frequent in states of drowsiness and NREM sleep (Gu et al.,
280 2021; Li et al., 2023; Liu et al., 2018; Raut et al., 2021). The vigilance-dependent FC patterns of
281 the arousal ROIs may be influenced by the occurrence of these global slow waves, which are
282 characterized by activation of sensory and motor cortices and co-deactivation of arousal nuclei
283 in the thalamus, brainstem, and basal forebrain (Gu et al., 2021; Liu et al., 2018). The gamma
284 power of intracranial EEG recordings in monkeys also exhibits a similar propagating wave
285 topology that has been linked to cortex-wide increases in low-frequency electrophysiological
286 activity, providing evidence for an electrophysiological basis (Gu et al., 2021; Li et al., 2023; Liu
287 et al., 2015; Raut et al., 2021).

288 The vigilance-dependent FC alterations of the arousal ROIs were reduced but not completely
289 removed when regressing out low-frequency physiological effects from the fMRI data. This
290 indicates that changes in respiration and heart rate are associated with some but not all of the
291 vigilance-dependent FC differences, which may be related to the role of the subcortical arousal
292 regions in central autonomic and cardiorespiratory regulation (Benarroch, 2018; Iacovella and
293 Hasson, 2011). Prior work has demonstrated that physiological effects in fMRI are greater at
294 lower vigilance levels and are strongly correlated with the global fMRI signal and with fMRI
295 signals in the thalamus, precuneus, and sensory and motor cortices (Gold et al., 2024; Ozbay et
296 al., 2019; Yuan et al., 2013). The precuneus and sensory cortices are brain areas with a high
297 vascular density (Bernier et al., 2018), suggesting that the physiological covariance in fMRI may
298 partially represent systemic effects on brain vasculature (e.g., due to changes in arterial CO_2
299 concentration and blood pressure) (Chen et al., 2020; Liu, 2016; Liu et al., 2017). However,
300 studies have shown that arousal-related global activity in fMRI co-occurs with shifts in both EEG
301 power and peripheral physiological signals (Gold et al., 2024; Gu et al., 2022; Ozbay et al.,
302 2019). Electrophysiological oscillations in sensory and autonomic brain regions have also been
303 observed to be coupled with cardiorespiratory activity, potentially reflecting neural interoceptive
304 and autonomic processes (Engelen et al., 2023; Herrero et al., 2018; Kluger and Gross, 2021).

305 The stronger global correlation pattern of the arousal ROIs in the drowsy state suggests that
306 neuromodulatory arousal systems may be involved in regulating global fMRI activity. These
307 findings agree with a previous study demonstrating that inactivation of the NBM leads to
308 suppression of global fMRI signals (Turchi et al., 2018). Neuromodulatory regulation of global
309 fMRI activity may occur through multiple, interconnected mechanisms. Global fMRI fluctuations
310 have been shown to be coupled to low-frequency electrophysiological oscillations and to low-
311 frequency variations in heart rate and respiration (Gu et al., 2022; Liu et al., 2018; Ozbay et al.,
312 2019; Pourmotabbed et al., 2024; Wong et al., 2013). These slow signal changes may be
313 influenced by neuromodulatory control of widespread neuronal activity, brain vasculature, and
314 autonomic function across different vigilance states. For instance, low-frequency EEG
315 oscillations during drowsiness and NREM sleep are thought to arise due to the influence of
316 decreased neuromodulator levels on thalamocortical activity (Brown et al., 2012; Lorincz and

317 Adamantidis, 2017). Neuromodulator levels also mediate brain vascular tone and astrocyte
318 activity, which can affect low-frequency electrophysiological signals via modification of interstitial
319 ion concentrations (Ding et al., 2016; Lewis, 2021; Rasmussen et al., 2020). In addition,
320 subcortical arousal regions are implicated in vigilance-dependent modulation of central
321 cardiorespiratory control (Benarroch, 2018), and fluctuations in peripheral physiological activity
322 are associated with systemic vascular effects (Chen et al., 2020; Liu, 2016; Liu et al., 2017) and
323 entrainment of neural activity (Engelen et al., 2023; Herrero et al., 2018; Kluger and Gross,
324 2021).

325 The most dominant connections of the static FC of the arousal ROIs were reproducible across
326 the three fMRI modalities and consisted of strong correlations to the thalamus, basal ganglia,
327 precuneus, sensory and motor cortices, and salience and default mode networks. These brain
328 areas partially align with the whole-brain structural connectivity profiles of the subcortical
329 arousal nuclei. The LC has dense projections to the thalamus, sensory and motor cortices,
330 precuneus, and salience and default mode networks (insula, cingulate gyrus, and medial
331 prefrontal cortex) as well as sparse projections to the basal ganglia (caudate and putamen)
332 (Zerbi et al., 2019). Studies in rodents have employed chemogenetic stimulation techniques to
333 demonstrate that LC projections influence the FC strength of these regions (Oyarzabal et al.,
334 2022; Zerbi et al., 2019). Moreover, our findings revealed that the static FC patterns were highly
335 similar across the brainstem ROIs and moderately similar between the brainstem and basal
336 forebrain ROIs. The similarity of the FC patterns may result from the reciprocal structural
337 connections of the arousal nuclei and from reciprocal modulation of their neurotransmitter
338 activity (Brown et al., 2012; Edlow et al., 2024).

339 We found that the arousal ROIs generally had strong FC to the precuneus and salience, default
340 mode, auditory, and sensorimotor networks in both the alert and drowsy states and strong FC to
341 the visual networks in the drowsy state. Prior studies have provided evidence for the importance
342 of neuromodulatory arousal systems in sensory processing (Mather et al., 2016; Poe et al.,
343 2020), which is consistent with the strong connectivity of the subcortical arousal nuclei to the
344 salience and sensory networks. For example, the LC-norepinephrine system has been
345 hypothesized to interact with the salience network in order to regulate selective processing of
346 salient stimuli (Mather et al., 2016; Poe et al., 2020). Norepinephrine and LC activity have also
347 been shown to alter visual field receptors in the occipital lobe, modulate odor detection, and
348 enhance auditory perception (Poe et al., 2020). Furthermore, monoaminergic neuromodulators
349 and the basal forebrain have been implicated in regulating neural activity and FC within the
350 default mode network (Harrison et al., 2022; Kelly et al., 2009; Nair et al., 2018; Oyarzabal et
351 al., 2022; van Wingen et al., 2014). The default mode network has been shown to be more
352 active during states of resting wakefulness compared to externally oriented tasks (Buckner and
353 DiNicola, 2019), and FC of the default mode network has been associated with behavioral and
354 electrophysiological measures of drowsiness (Chang et al., 2013; Samann et al., 2011; Ward et
355 al., 2013). In our work, the FC patterns of the arousal ROIs had greater spatial overlap with the
356 dorsal default mode network at a higher vigilance state, indicating that interactions between the
357 arousal nuclei and default mode network may be involved in promoting a resting wakeful state.

358 Unsupervised clustering of the dynamic FC of the arousal ROIs resulted in state-dependent FC
359 patterns that were highly reproducible between the VU 3T-ME and HCP 7T datasets. The FC in

10

360　the lower vigilance state was characteristic of the sensory dominated global correlation pattern
361　observed in the EEG-derived drowsy state while the FC in the higher vigilance state exhibited
362　strong correlations to the thalamus, precuneus, and salience and default mode networks. The
363　global FC pattern corresponded to a lower EEG vigilance score in the VU 3T-ME dataset and to
364　a greater percent eye closure in the HCP 7T dataset, which is consistent with the similarity of
365　vigilance-fMRI relationships between EEG-fMRI and pupillometry-fMRI modalities (Liu and
366　Falahpour, 2020; Soon et al., 2021). Pupil size and dilation are indices of increased arousal and
367　have been shown to be negatively correlated with fMRI signals in sensorimotor and visual
368　networks and positively correlated with thalamic and brainstem regions (Murphy et al., 2014;
369　Schneider et al., 2016; Yellin et al., 2015). Spontaneous eye closures are indices of decreased
370　arousal and have been associated with fMRI activation in the precuneus and ventral default
371　mode, auditory, sensorimotor, and visual networks and with deactivation in the thalamus and
372　brainstem (Ong et al., 2015; Soon et al., 2021). The fMRI activation patterns during eye
373　closures resemble the spatial topology of global fMRI waves that occur more often at lower
374　vigilance levels (Gu et al., 2021; Li et al., 2023; Liu et al., 2018; Raut et al., 2021). These
375　arousal-related brain activation events may influence the dynamic FC profiles of the subcortical
376　arousal nuclei, which have been implicated in regulating pupil activity across different vigilance
377　states (Joshi, 2021; Larsen and Waters, 2018).

378　Our findings for the static FC patterns of the arousal ROIs generally agree with the results of
379　prior studies (Bar et al., 2016; Beliveau et al., 2015; Li et al., 2014; Turker et al., 2021; Yuan et
380　al., 2019; Zhang et al., 2016), although some discrepancies are observed primarily in the
381　sensorimotor and visual networks. Inconsistencies between datasets may be a consequence of
382　differences in tSNR, preprocessing strategies, sample size, and vigilance state (e.g., eyes-
383　closed versus eyes-open and shorter versus longer scan durations). Previous work in fMRI
384　found that the FC of the LC is only moderately concordant between multi-echo and single-echo
385　preprocessed fMRI data (Turker et al., 2021). In our study, the tSNR of the arousal ROIs in the
386　multi-echo fMRI dataset was greater than the tSNR in both the 3T and 7T single-echo fMRI
387　datasets even though ICA-FIX had been applied to mitigate non-BOLD artifacts. Additionally, we
388　found that the aCompCor pipeline reduced the overall strength of the FC maps, introduced
389　significant negative correlations for the HCP datasets, and resulted in lower cross-modality
390　reproducibility. Similarly, previous studies that employed aCompCor or global signal regression
391　observed significant negative correlations in the FC patterns of the LC, DR, VTA, and NBM
392　(Beliveau et al., 2015; Li et al., 2014; Zhang et al., 2016). Global signal regression and
393　aCompCor aggressively remove global contributions to the correlation profiles of the arousal
394　ROIs, and global signal regression has been shown to shift FC networks in fMRI toward
395　negative correlations (Murphy and Fox, 2017). These negative correlations may be a byproduct
396　of removing vigilance-related signals from the fMRI data (Liu et al., 2017; Nalci et al., 2017).

397　The cross-modality reproducibility of the static FC was the lowest for the VTA, PAG, and
398　MS/DBB. The VTA had the lowest tSNR of the arousal ROIs in all three datasets, and the PAG
399　may be more susceptible to non-neural influences because of its proximity to the cerebral
400　aqueduct. We implemented ME-ICA in the VU 3T-ME dataset and ICA-FIX in the HCP datasets
401　to mitigate non-BOLD cyclic physiological artifacts, and we evaluated the FC after regressing
402　out low-frequency physiological effects modeled from WM and CSF signals (mCSF/WM and

403   aCompCor pipelines) or heart rate and respiration signals (physio pipeline). Other studies have
404   implemented similar preprocessing strategies (e.g., RETROICOR and removal of WM and CSF
405   regressors) (Bar et al., 2016; Beliveau et al., 2015; Turker et al., 2021; Yuan et al., 2019).
406   However, the optimal preprocessing pipeline remains an open question and may include novel
407   techniques, such as masked ICA (Beissner, 2015; Maki-Marttunen and Espeseth, 2021).
408   Advanced methods for localization and co-registration of the arousal ROIs, such as deep
409   learning-based segmentation and contrast enhanced structural imaging, may also improve the
410   accuracy of the FC estimates (Doss et al., 2023; Maki-Marttunen and Espeseth, 2021; Turker et
411   al., 2021). An important caveat is that aggressive removal of low-frequency physiological effects
412   during preprocessing may reduce meaningful signal variance associated with arousal-related
413   neural and neuromodulatory activity. In particular, studies have shown that low-frequency EEG
414   oscillations are coupled to slow pulsations in global fMRI activity, CSF flow, respiration, and
415   cardiac signals during low vigilance states, which may reflect arousal-related metabolic
416   clearance and autonomic processes (Fultz et al., 2019; Helakari et al., 2022; Picchioni et al.,
417   2022).

418   The static FC patterns of the arousal ROIs had a moderate to good reproducibility across the
419   three fMRI modalities despite the lower tSNR of the HCP datasets compared to the VU 3T-ME
420   dataset. The large sample size of the HCP datasets and greater number of timepoints per
421   subject provide greater statistical power that may compensate for the lower tSNR (Helwegen et
422   al., 2023; Smith et al., 2013). In addition, the static FC in the 3T and 7T HCP datasets tended to
423   have higher reproducibility with each other than with the VU 3T-ME dataset, which may be
424   attributed to several factors. Both the HCP datasets were collected in an eyes-open condition
425   (rather than the eyes-closed condition in the VU 3T-ME dataset) and were acquired with a multi-
426   band fMRI sequence. The HCP datasets also share some of their subject population and have a
427   similar age range. The neocortical FC of subcortical arousal regions has been shown to be
428   associated with age and age-related cognitive performance (Guardia et al., 2022).

429   Overall, the results of our study suggest that the FC of most of the arousal ROIs is influenced by
430   dynamic variations in vigilance state. The spatial topology of the vigilance-dependent FC may
431   reflect the role of the arousal nuclei in regulating global fMRI activity via neurobiological,
432   autonomic, and vascular mechanisms. These findings have broad implications for studying
433   arousal networks in healthy individuals and for clinical investigations of disrupted arousal circuits
434   in neurological and neuropsychiatric disorders. Degeneration of cholinergic and monoaminergic
435   neurons is a hallmark of neurodegenerative disorders such as Parkinson's and Alzheimer's
436   disease (Grothe et al., 2014; Kelberman et al., 2020; Ray et al., 2018; Schmitz et al., 2016;
437   Seidel et al., 2015), and the fMRI activity and FC of brainstem and basal forebrain nuclei have
438   been related to cognitive outcomes in these disease groups (Mieling et al., 2023; Serra et al.,
439   2018; Wang et al., 2023; Zeng et al., 2022). Impaired FC of subcortical arousal regions has also
440   been observed in temporal lobe epilepsy (Englot et al., 2018; Gonzalez et al., 2023; Gonzalez et
441   al., 2021) and traumatic brain injury (Snider et al., 2020; Spindler et al., 2021; Woodrow et al.,
442   2023) and may contribute to excessive drowsiness, sleep disturbances, and neurocognitive
443   deficits of attention and executive function (Englot et al., 2020; Sandsmark et al., 2017).
444   However, if not properly controlled for, differences in vigilance between patient and control
445   populations can act as a confounding factor in resting-state neuroimaging studies. Likewise,

446   modeling vigilance-related interactions in fMRI may lead to the discovery of novel neural and

447   physiological biomarkers of arousal and neurocognitive disturbances (Bagshaw et al., 2017;

448   Guo et al., 2023; Wang et al., 2024).

4. METHODS

4.1. Simultaneous EEG-fMRI data collection and preprocessing

451   This study included resting-state fMRI data from three datasets. Detailed descriptions of the

452   datasets are provided in **Table 1.** The first dataset consisted of 20-minute sessions of 3T multi-

453   echo fMRI collected from 36 healthy subjects (65 sessions in total) during April 1, 2021 to April

454   29, 2023 at Vanderbilt University (VU 3T-ME dataset). All the participants provided written

455   informed consent, and the study protocol was approved by the Institutional Review Board of

456   Vanderbilt University. The MRI data were acquired on a Philips 3T Elition X scanner (Philips

457   Healthcare, Best, Netherlands) with a 32-channel head/neck coil. The BOLD fMRI data were

458   collected in an eyes-closed resting-state condition with a 3T multi-echo, gradient-echo EPI

459   sequence (3-mm by 3-mm in-plane ACQ resolution; 2.5-mm by 2.5-mm in-plane reconstruction

460   resolution; 240-mm by 240-mm in-plane FOV; slice thickness = 3 mm; slice gap = 1 mm; 30

461   axial slices; FA = 79°; TE = 13, 31, 49 ms; TR = 2100 ms; N = 575 volumes). A high-resolution,

462   T1-weighted structural volume was obtained for anatomical co-registration with a multi-shot,

463   turbo-field-echo sequence (1-mm isotropic spatial resolution; 256-by-256 in-plane FOV; 150

464   axial slices; FA = 8°; minimum TI delay = 634.8 ms; TE = 4.6 ms; TR = 9 ms; turbo factor =

465   128).

466   Scalp EEG, respiratory, and photoplethysmography (PPG) data were recorded simultaneously

467   with the fMRI data. MRI scanner (volume) triggers were recorded with the EEG and

468   physiological signals for data synchronization. The scalp EEG data were collected with a 32-

469   channel 3T MR compatible system (BrainAmps MR, Brain Products GmbH) at a sampling rate

470   of 5 kHz, referenced to the FCz channel, and synchronized to the scanner's 10 MHz clock. The

471   respiratory and PPG data were collected at a 496 Hz sampling rate using a pneumatic belt and

472   PPG transducer integrated with the MR scanner (Philips Healthcare, Best, Netherlands). The

473   pneumatic belt was placed around the subject's abdomen, and the PPG transducer was

474   attached to the subject's index finger. Data from 15 sessions were excluded due to the

475   presence of buffer overflow errors, data transfer artifacts, or excessive noise (e.g., unremoved

476   residual gradient artifacts) in the EEG data. Data from 5 sessions were excluded due to missing

477   fMRI volumes and/or abbreviated scanning sessions. All the remaining 30 subjects (15 subjects

478   with 2 sessions and 15 subjects with 1 session; 45 sessions in total) were included in the study.

479   Out of the remaining subjects, 2 of the subjects (4 sessions) had unusable respiratory and PPG

480   recordings and were excluded from any analyses requiring use of the physiological data.

481   The 3T multi-echo fMRI data were preprocessed in AFNI (https://afni.nimh.nih.gov) using the

482   following procedure: motion co-registration with six-parameter rigid body alignment based on

483   the middle echo (3dvolreg function), slice-timing correction (3dTshift function), and denoising

484   with multi-echo independent component analysis (ME-ICA) (tedana 0.0.9a toolbox). ME-ICA

485   was performed to mitigate non-neuronal artifacts in the fMRI data caused by head motion and

486   aliased cyclic physiological noise resulting from cardiac pulsatility and respiration-induced B0-

487   field shifts (Kundu et al., 2013; Kundu et al., 2012; Turker et al., 2021). After the ME-ICA

488 denoising, the fMRI data were co-registered to the structural T1-weighted image and nonlinearly
489 warped to the MNI152 template (2-mm isotropic resolution) using the Advanced Normalization
490 Tools (ANTs) toolbox (https://github.com/ANTsX/ANTs). Additional preprocessing of the
491 normalized fMRI data included spatial smoothing at FWHM = 3 mm (AFNI 3dFWHMx function),
492 confound regression of potential noise signals (described in section 4.4) and Legrende
493 polynomials up to 4th order (to remove scanner drift), and bandpass filtering at 0.01-0.15 Hz.

494 The EEG data were denoised using the average artifact subtraction procedure of BrainVision
495 Analyzer 2 (Brain Products, Munich, Germany) to remove MR-induced gradient and
496 ballistocardiogram (BCG) artifacts (Goodale et al., 2021). The EEG data were then aligned to
497 the fMRI data, down-sampled to 250 Hz, and additionally preprocessed with the EEGLAB
498 v2020.0 toolbox of MATLAB. The additional preprocessing steps included 60 Hz notch filtering
499 to remove powerline noise, 0.5 high-pass and 70 Hz lowpass filtering, and rejection of noisy
500 channels (e.g., exhibiting low correlation to neighboring electrodes). The bad channel rejection
501 was limited to at most 3 channels. After the preprocessing, the Vigilance Algorithm Leipzig
502 (VIGALL) algorithm was implemented to stage the EEG data into five vigilance stages
503 (described in section 4.5) (Sander et al., 2015).

504 The respiratory data of the subjects were contaminated with transient periods of signal dropout
505 due to malfunction of the transducer. These periods were visually marked and replaced with
506 NaN values to denote missing time points (3.4-6.4% [IQR] of the total scan duration). The
507 respiratory volume (RV) time-series, matched to the fMRI sampling rate, was then computed by
508 calculating the temporal standard deviation of the respiratory waveform in 6-s sliding windows
509 centered at each TR (Chang et al., 2009; Chen et al., 2020). The RV at each time window was
510 calculated using all the available time points in the window if less than 20% of the time points
511 were missing. The RV was assigned a NaN value otherwise. For the PPG data, the peak
512 detection algorithm of MATLAB (findpeaks function) was used to locate time points
513 corresponding to individual heart beats, and the time-varying inter-beat-interval was computed
514 by calculating the difference between adjacent peak times (Chang et al., 2009; Chen et al.,
515 2020). Outliers in the inter-beat-interval time-course were identified based on a cut-off of more
516 than 2.5 standard deviations away from the mean and linearly interpolated (0.75-1.8% [IQR]
517 outliers out of all the time points per session). The heart rate (HR) time-series was then
518 computed by calculating the inverse of the median inter-beat-interval in 6-s sliding windows
519 centered at each TR.

520 **4.2. Human Connectome Project (HCP) database and preprocessing**

521 The other two datasets included in this study consisted of a subsample of healthy subjects with
522 3T single-echo fMRI (HCP 3T dataset) and a subsample of healthy subjects with 7T single-echo
523 fMRI (HCP 7T dataset) from the HCP S1200 data release (Smith et al., 2013; Van Essen et al.,
524 2012). Respiratory and PPG data were simultaneously acquired in the HCP 3T dataset, and
525 pupillometry data were simultaneously acquired in the HCP 7T dataset. For the HCP 3T
526 dataset, we included subjects (n = 375 subjects; 1500 sessions in total) who had four complete
527 14.4-minute sessions of resting-state fMRI data and whose physiological recordings were
528 previously reported to be of good quality (Power et al., 2020; Xifra-Porxas et al., 2021). For the

529   HCP 7T dataset, we included subjects (n = 176 subjects; 704 sessions in total) who had four
530   complete 15-minute sessions of resting-state fMRI data.

531   For both HCP datasets, the fMRI data were acquired in an eyes-open resting-state condition
532   using a simultaneous multi-slice, gradient-echo EPI pulse sequence. The imaging parameters
533   were 2-mm isotropic spatial resolution, FA = 52°, TE = 33.1 ms, TR = 720 ms, multiband factor
534   = 8, N = 1200 volumes for the HCP 3T dataset and 1.6-mm isotropic spatial resolution, FA =
535   45°, TE = 22.2 ms, TR = 1000 ms, multiband factor = 5, N = 900 volumes for the HCP 7T
536   dataset. The data were provided after prior preprocessing had been performed with the ICA-FIX
537   denoising pipeline (Smith et al., 2013). Briefly, the ICA-FIX pipeline included distortion and
538   motion correction, co-registration to the subject's structural T1-weighted image, global intensity
539   normalization, spatial normalization to the standard MNI space, minimal high-pass filtering
540   (cutoff = 2000 s), and ICA with the FSL tool FIX to remove non-neural spatiotemporal
541   components (e.g., corresponding to scanner drift, head motion, and cyclic physiological noise).
542   We additionally preprocessed the ICA-FIX cleaned data using the following procedure. The
543   HCP 7T fMRI data were spatially down-sampled to a 2-mm isotropic resolution to match the
544   spatial resolution of the other two datasets, and the fMRI data of both HCP datasets were
545   spatially smoothed at FWHM = 4 mm (AFNI 3dFWHMx function), bandpass filtered at 0.01-0.15
546   Hz, and temporally down-sampled by a factor of 2. Confound regression of potential noise
547   signals (described in section 4.4) was then performed on the bandpass filtered and down-
548   sampled fMRI data.

549   RV and HR signals were computed from the respiratory and PPG data in the HCP 3T dataset
550   following the same sliding window procedure described in section 4.1. The RV and HR signals
551   were then bandpass filtered at 0.01-0.15 Hz and temporally down-sampled by a factor of 2. In
552   the HCP 7T dataset, the pupillometry data were aligned to the fMRI data and screened for faulty
553   recordings according to the methodology of Gonzalez-Castillo et al (Gonzalez-Castillo et al.,
554   2022). Out of 704 sessions, 568 had available pupillometry data. Out of these 568 sessions, the
555   pupillometry data of 20 sessions lacked TR onset information, had abbreviated recordings, or
556   could not be loaded. Another 26 sessions had periods of eye closure greater than 90% of the
557   recording duration, indicating potentially defective eye tracking. These 46 sessions were
558   excluded from any analyses requiring use of the pupillometry data, leaving a total of 522
559   sessions (145 subjects).

4.3. Brain regions of interest

561   Seed regions-of-interest (ROIs) were defined as the 9 brainstem ROIs of the Harvard Ascending
562   Arousal Network (AAN) atlas Version 1.0 (https://www.nmr.mgh.harvard.edu/resources/aan-
563   atlas) (Edlow et al., 2024; Edlow et al., 2012) and the 2 bilateral basal forebrain ROIs of the
564   JuBrain Anatomy Toolbox (https://www.fz-juelich.de/en/inm/inm-7/resources/jubrain-anatomy-
565   toolbox) (Zaborszky et al., 2008). The brainstem ROIs consist of monoaminergic, glutamatergic,
566   and cholinergic nuclei of the ascending reticular activating system (ARAS) involved in regulating
567   wakefulness, alertness, and autonomic function (Scammell et al., 2017). The basal forebrain
568   ROIs consist of cholinergic nuclei involved in cortical activation and autonomic integration
569   (Scammell et al., 2017). A more detailed description of the seed regions is provided in **Table 2**.

570   For all three datasets, time-courses for the seed regions were extracted by averaging across the
571   time-series of all the voxels in each ROI. The ROI extraction was performed on the fMRI data at
572   the original spatial resolution in the MNI space (i.e., 2-mm for the VU 3T-ME and HCP 3T
573   datasets and 1.6-mm for the HCP 7T dataset) without the spatial smoothing step, without the
574   spatial down-sampling step (HCP 7T dataset), and before the confound regression pipelines
575   (described in section 4.4). In order to evaluate the quality of the BOLD signal in each seed
576   region, the temporal SNR (tSNR) of the seed time-courses was computed by calculating the
577   mean of the time-course divided by the standard deviation. The standard deviation was
578   computed for the ICA-FIX denoised signals in the HCP datasets (which includes drift removal
579   and minimal high-pass filtering) and for the ME-ICA denoised and detrended signals in the VU
580   3T-ME dataset. The tSNR of the seed regions was compared to the tSNR of ROIs from the
581   Schaefer cortical atlas (200 ROIs, 17 brain networks) (Schaefer et al., 2018) and Melbourne
582   subcortical atlas (32 ROIs) (Tian et al., 2020). For use in the later confound regression
583   pipelines, physiological tissue-based signals were extracted and included mean time-courses of
584   the white matter (WM), deep cerebrospinal fluid (CSF) (i.e., first, second, and third ventricles),
585   and fourth ventricle (FV). Masks for the gray matter (GM), WM, and CSF were obtained from the
586   tissue-type probability maps available in FSL (https://fsl.fmrib.ox.ac.uk/fsl; 35% threshold for the
587   GM, 50% threshold for the CSF, and 90% threshold for the WM).

588   **4.4. Static functional connectivity analysis**

589   Static FC patterns were estimated by computing the seed-based correlation of each brainstem
590   and basal forebrain ROI to the voxels of the entire brain over the entire fMRI scan duration. The
591   seed-based correlation was calculated after additional preprocessing was performed with three
592   different confound regression pipelines (i.e., the mCSF/WM pipeline, aCompCor pipeline, and
593   physio pipeline) (Caballero-Gaudes and Reynolds, 2017). The mCSF/WM pipeline involved
594   regression of the mean WM, deep CSF, and FV signals (Turker et al., 2021); the anatomical
595   CompCor (aCompCor) pipeline involved regression of the first five principal components of the
596   mean WM and deep CSF signals (Behzadi et al., 2007); and the physio pipeline involved
597   regression of low-frequency physiological effects modeled from the RV and HR signals
598   convolved with five respiratory and five cardiac response functions (Chen et al., 2020). Before
599   the confound regression, missing values in the convolved RV signals due to transducer
600   malfunction were replaced with 0's in the regression matrix.

601   Signals from the WM and deep CSF may contain a mixture of neuronal and non-neuronal
602   influences (e.g., motion and systemic vascular effects) and are often removed from the fMRI
603   data (Caballero-Gaudes and Reynolds, 2017). The FV is in close proximity to several of the
604   brainstem nuclei and may capture non-neuronal contamination in the seed time-courses (Turker
605   et al., 2021). Likewise, the low-frequency physiological regressors may capture non-neuronal
606   influences due to systemic vascular effects (e.g., changes in arterial pressure and CO_2
607   concentration) (Brooks et al., 2013; Chen et al., 2020). However, the physiological regressors
608   may also covary with neuronal activity in the central nervous system involved in autonomic
609   regulation, and regression of these signals may be detrimental to analysis of nuclei in the
610   brainstem and basal forebrain (Chen et al., 2020). Therefore, we sought to characterize the
611   impact of these preprocessing techniques on the FC of the seed regions. Global signal
612   regression was not performed considering that neuromodulatory systems in the brainstem and

613 basal forebrain may be potential neuronal contributors of global signal fluctuations in resting-
614 state fMRI (Turchi et al., 2018; Turker et al., 2021).

615 For each dataset, the voxel-wise correlation values were converted to z-scores with Fisher's r-
616 to-z transformation, and linear mixed-effects (LME) models were fitted to the z-transformed
617 correlation values across all the fMRI sessions using the REML method (Chen et al., 2013). The
618 LME model per voxel was specified with the following formula:

$$r_{ij} = \mu + \delta_i + \epsilon_{ij}$$

619 where r_{ij} is the correlation value for subject i and session j, μ represents the group average
620 correlation value across all subjects, δ_i is a random intercept term modeling the inter-subject
621 variance, and ϵ_{ij} is the residual error term modeling the intra-subject variance. We then derived
622 t-scores for the group average correlation from the LME models. To identify brain regions with
623 the strongest correlation to the seed ROIs, the t-maps were thresholded at 40% of the top t-
624 values in the GM and at $p < 0.05$ (voxel-wise false-discovery rate [FDR]-corrected over the
625 entire GM volume). The spatial reproducibility of the thresholded t-maps between each pair of
626 datasets and each pair of preprocessing pipelines was evaluated using the Dice similarity
627 coefficient (DSC) (Turker et al., 2021). The multiclass generalization of the DSC was
628 implemented to account for positive and negative t-values in the t-maps (Taha and Hanbury,
629 2015). The reproducibility was scored as poor (DSC < 0.4), moderate (0.4 ≤ DSC < 0.6), and
630 good (DSC ≥ 0.6).

631 For ease of visualization of the whole-brain FC patterns of the seed ROIs, we computed the
632 spatial overlap of their thresholded FC t-maps with 16 canonical brain network templates from
633 the FINDLAB and Melbourne atlases (Shirer et al., 2012; Tian et al., 2020). The spatial overlap
634 values of each t-map were quantified with the Szymkiewicz-Simpson coefficient for the positive
635 and negative t-values separately, and a signed version of the overlap coefficient was derived by
636 taking the difference between the overlap coefficients of the positive and negative t-values.

4.5. EEG-based vigilance-dependent connectivity analysis

638 The simultaneous EEG data in the VU 3T-ME dataset provides a gold standard method of
639 identifying time periods of alertness and drowsiness according to the spatial distribution of
640 power changes in different frequency bands (Oken et al., 2006; Olbrich et al., 2009). For
641 example, periods of alertness during relaxed wakefulness are characterized by dominant alpha
642 power in the occipital region, and periods of drowsiness are characterized by greater power in
643 the delta and theta bands (Olbrich et al., 2009). The VIGALL algorithm is an automated method
644 for classification of scalp EEG into vigilance stages based on these spatial power distributions
645 (Huang et al., 2015; Jawinski et al., 2019; Sander et al., 2015). In this study, the VIGALL 2.1
646 add-on of Brain Vision Analyzer 2 was implemented to stage each 1 second epoch of the
647 preprocessed EEG data into five vigilance stages (i.e., A1, A2, A3, B1, B2/3) corresponding to
648 decreasing levels of alertness. Before the vigilance staging, spherical spline interpolation was
649 used to reconstruct EEG channels in the VIGALL standard that were not present in the data,
650 and the EEG signals were re-referenced to the common average.

651 The staged EEG data were segmented into epochs of 63-s duration (30 TRs; 19 epochs per
652 session), and a custom algorithm was used to assign each epoch into one of three vigilance
653 states (i.e., alert, intermediate, or drowsy). First, the five VIGALL stages were converted to
654 integer values from 1 (most drowsy) to 5 (most alert), and the Wilcoxon signed-rank test was
655 applied to the integer values of each epoch to test for a significant difference of the median
656 away from a (weighted) center value of 2.75. Next, a threshold of ±1.5 for the z-statistic of the
657 signed-rank test was used to assign epochs to the three vigilance states, and adjacent epochs
658 belonging to the same state were concatenated. The epochs were then shifted forward by 5
659 seconds (~2 TRs) to account for the temporal delay between the peak BOLD response and
660 neural activity. Our algorithm identified 21 subjects with alert epochs (n = 51 epochs; 178 ± 215
661 TRs per epoch) and 25 subjects with drowsy epochs (n = 75 epochs; 191 ± 208 TRs per epoch).
662 The accuracy of the vigilance staging algorithm was assessed by comparing the alert and
663 drowsy classifications with a previously validated quantitative index of vigilance (i.e., the EEG
664 alpha/theta power ratio) (Goodale et al., 2021; Oken et al., 2006). The U-Sleep deep learning
665 algorithm was also used to perform automatic sleep staging of the EEG data (Perslev et al.,
666 2021), and we determined that the drowsy epochs primarily consisted of awake drowsy and light
667 sleep (N1/N2) stages.

668 We then employed the EEG-derived vigilance states to investigate the vigilance-dependent FC
669 of the seed regions in the fMRI data for each pipeline. The seed-based correlation of the
670 brainstem and basal forebrain ROIs was computed for each alert and drowsy epoch, and two-
671 state LME models were fitted to the voxel-wise correlation values across all the epochs after
672 applying Fisher's r-to-z transformation. The two-state LME models were specified with the
673 following formula:

$$r_{ij} = \alpha_0 + \alpha_1 \cdot c_{ij} + \beta \cdot x_{ij} + \delta_i + \epsilon_{ij}$$

674 where r_{ij} is the correlation value for subject i and epoch j, α_0 is the fixed intercept, α_1 represents
675 the fixed effect of vigilance state c_{ij} (i.e., alert or drowsy), and β represents a fixed slope
676 covarying for the number of TRs per epoch x_{ij}. We then derived t-scores for the fixed effect of
677 vigilance state (referenced to the alert state) from the two-state LME models. For each state
678 separately, single-state LME models were also fitted to the z-transformed correlation values:

$$r_{ij} = \mu + \beta \cdot x_{ij} + \delta_i + \epsilon_{ij}$$

679 where μ represents the group average correlation value across all subjects in a single vigilance
680 state. We derived t-scores for the group average correlation from the single-state LME models.
681 The t-maps for the two- and single-state models were thresholded at 40% of the top t-values in
682 the GM and at $p < 0.05$ (voxel-wise FDR-corrected over the entire GM volume). The DSC was
683 then used to evaluate the spatial reproducibility of the two- and single-state t-maps between the
684 mCSF/WM, physio, and aCompCor pipelines.

685 **4.6. Pupillometry-based state-dependent connectivity analysis**

686 The simultaneous eye-tracking recordings in the HCP 7T dataset provide a measure of vigilance
687 and autonomic activity (Schneider et al., 2016; Wang et al., 2016). Previous studies have
688 suggested that periods of drowsiness result in increased blink duration and more frequent and

689 longer periods of extended eye closure (Abe, 2023; Shekari Soleimanloo et al., 2019; Soon et
690 al., 2021). However, unlike scalp EEG, analysis of eye-tracking data does not have a clear
691 method for automatic identification of alert and drowsy periods, and zero pupil diameter values
692 may be confounded by instances of voluntary eye closure or device malfunction. Therefore, we
693 characterized the state-dependent FC of the seed regions in an unsupervised manner (Wang et
694 al., 2016), and we compared the FC patterns between the VU 3T-ME and HCP 7T datasets for
695 the mCSF/WM pipeline.

696 The seed-based correlation of the brainstem and basal forebrain ROIs in the HCP 7T dataset
697 was computed for sliding time windows of 4-minute duration and 50% overlap, and the
698 correlation values were converted to z-scores with Fisher's r-to-z transformation. For each ROI,
699 the dynamic whole-brain correlation patterns were concatenated across all the 522 sessions
700 with available pupillometry data, and k-means clustering was employed to spatially cluster the
701 correlation patterns into different states. The distance metric was chosen to be the cityblock
702 distance according to the recommendation of previous fMRI studies (Allen et al., 2014), and the
703 optimal number of clusters (k = 2) was selected based on the silhouette and variance ratio
704 criteria for a representative ROI (i.e., the LC). For the LC, the clustering analysis was repeated
705 for window sizes of 1-minute duration. However, because no appreciable difference was
706 observed between the clustering results for the different window sizes, 4-minute windows were
707 selected for computational efficiency.

708 The percent duration of eye closure was computed for each sliding window after applying a
709 forward shift of 4 seconds to account for the temporal delay between the peak pupil and BOLD
710 response to neural activity (Schneider et al., 2016). The percent eye closure was calculated
711 based on the proportion of missing (zero) pupil diameter values in each 4-minute window and
712 includes periods of blinking and prolonged eye closure. A two-state LME model was fitted to the
713 percent eye closure values across all the time windows to test for a significant effect of state
714 (referenced to state 1) after applying a logit transformation to ensure normality.

715 The dynamic FC analysis (4-min sliding windows, 50% overlap) and k-means clustering
716 procedure (k = 2) was repeated for each seed region in the VU 3T-ME dataset. The VIGALL-
717 based alert/drowsy staging algorithm (described in section 4.5) was applied to the EEG data in
718 each sliding window to derive scores of vigilance (i.e., z-scores), and a two-state LME model
719 was fitted to test for a significant effect of state on the vigilance scores. The proportion of
720 windows in each state that were classified as alert or drowsy was also computed after
721 thresholding the vigilance z-scores at ±1.5.

722 For both the HCP 7T and VU 3T-ME datasets, LME models were fitted to the voxel-wise
723 dynamic correlation values of each seed region to derive t-maps for the effect of state (state 2
724 versus 1) on the correlation values and t-maps for the group average correlation in each state
725 separately. The t-maps were thresholded at 40% of the top t-values in the GM and at p < 0.05
726 (voxel-wise FDR-corrected over the entire GM volume). The DSC was then used to evaluate the
727 spatial reproducibility of the two- and single-state t-maps between the HCP 7T and VU 3T-ME
728 datasets.

729

730 **Conflicts of Interest**

731 The authors declare no conflicts of interest.

732

733 **Acknowledgements**

740

741 **Funding**

743
744

FIGURE CAPTIONS

Fig. 1. Static functional connectivity of the subcortical arousal nuclei. (a) Static functional connectivity (FC) t-maps of the locus coresuleus (LC), cuneiform/subcuneiform nucleus (CSC), and nucleus basalis of Meynert (NBM) in the VU 3T-ME, HCP 3T, and HCP 7T datasets for the mCSF/WM preprocessing pipeline. The FC t-maps were thresholded at 40% of the top t-values in the gray matter and at p < 0.05 (voxel-wise false discovery rate [FDR]-corrected over the entire gray matter volume). AFNI was used for visualization of the t-maps (@chauffeur_afni function; upper functional range set to the 98th percentile). (b) Spatial overlap of the thresholded static FC t-maps of the subcortical arousal regions with 16 canonical brain network templates from the FINDLAB and Melbourne atlases (Shirer et al., 2012; Tian et al., 2020). (c) Spatial reproducibility (Dice similarity coefficient) of the thresholded static FC t-maps between the three fMRI datasets.

Fig. 2. Vigilance-dependent functional connectivity of the subcortical arousal nuclei. (a) An adapted version of the Vigilance Algorithm Leipzig (VIGALL) algorithm was used to perform automatic vigilance staging of the simultaneous EEG recordings in the VU 3T-ME dataset (Huang et al., 2015; Jawinski et al., 2019; Sander et al., 2015). The accuracy of the algorithm was assessed by comparing the alert and drowsy classifications with a previously validated quantitative index of vigilance (i.e., the EEG alpha/theta power ratio) (Goodale et al., 2021; Oken et al., 2006). (b) Vigilance-dependent functional connectivity (FC) t-maps of the locus coresuleus (LC), cuneiform/subcuneiform nucleus (CSC), and nucleus basalis of Meynert (NBM) in the VU 3T-ME dataset for the mCSF/WM preprocessing pipeline. The FC t-maps were thresholded at 40% of the top t-values in the gray matter and at p < 0.05 (voxel-wise false discovery rate [FDR]-corrected over the entire gray matter volume). AFNI was used for visualization of the t-maps (@chauffeur_afni function; upper functional range set to the 98th percentile). (c) Spatial overlap of the thresholded vigilance-dependent FC t-maps of the subcortical arousal regions with 16 canonical brain network templates from the FINDLAB and Melbourne atlases (Shirer et al., 2012; Tian et al., 2020).

Fig. 3. Cross-modality reproducibility of the vigilance-dependent functional connectivity. (a-b) State-dependent functional connectivity (FC) t-maps of the locus coreuleus (LC) and nucleus basalis of Meynert (NBM) in the VU 3T-ME and HCP 7T datasets for the mCSF/WM preprocessing pipeline. Unsupervised clustering of the dynamic whole-brain correlation patterns of each subcortical arousal nuclei was used to derive the two states. The FC t-maps were thresholded at 40% of the top t-values in the gray matter and at p < 0.05 (voxel-wise false discovery rate [FDR]-corrected over the entire gray matter volume). AFNI was used for visualization of the t-maps (@chauffeur_afni function; upper functional range set to the 98th percentile). (c) Comparison of vigilance metrics (i.e., EEG vigilance score in the VU 3T-ME dataset and percent eye closure in the HCP 7T dataset) between the two states. Asterisks indicate a significant difference at ***p < 1e-3 (FDR-corrected across the six subcortical arousal regions). (d) Spatial reproducibility (Dice similarity coefficient) of the thresholded state-dependent FC t-maps between the VU 3T-ME and HCP 7T datasets.

SUPPLEMENTARY FIGURE CAPTIONS

Supplementary Fig 1. Temporal signal-to-noise ratio (tSNR) of the brain regions-of-interest (ROIs) in the VU 3T-ME, HCP 3T, and HCP 7T datasets. The tSNR is averaged over all the subjects in each fMRI dataset, and the boxplots depict the distribution of the tSNR across the ROIs. The arousal ROIs include 9 brainstem regions from the Harvard Ascending Arousal Network (AAN) atlas Version 1.0 (Edlow et al., 2024; Edlow et al., 2012) and two bilateral basal forebrain regions from the Jubrain Anatomy Toolbox (Zaborszky et al., 2008). The cortical ROIs are defined from the Schaefer atlas (200 ROIs, 17 networks) (Schaefer et al., 2018), and the subcortical ROIs are defined from the Melbourne atlas (32 ROIs) (Tian et al., 2020).

Supplementary Fig 2. (a-b) Static functional connectivity (FC) of the subcortical arousal regions with each other in the VU 3T-ME, HCP 3T, and HCP 7T datasets for the mCSF/WM preprocessing pipeline. The FC is depicted as the Pearson correlation averaged across all the subjects in each dataset and as t-values derived for the group average correlation in each dataset. (c) Spatial similarity (Dice similarity coefficient) of the whole-brain static FC t-maps of the subcortical arousal ROIs with each other.

Supplementary Fig. 3. (a, c) Static functional connectivity (FC) t-maps of the locus coresuleus (LC), cuneiform/subcuneiform nucleus (CSC), and nucleus basalis of Meynert (NBM) in the VU 3T-ME, HCP 3T, and HCP 7T datasets for the physio and aCompCor preprocessing pipelines. The FC t-maps were thresholded at 40% of the top t-values in the gray matter and at $p < 0.05$ (voxel-wise false discovery rate [FDR]-corrected over the entire gray matter volume). AFNI was used for visualization of the t-maps (@chauffeur_afni function; upper functional range set to the 98th percentile). (b, d) Spatial overlap of the thresholded static FC t-maps of the subcortical arousal regions with 16 canonical brain network templates from the FINDLAB and Melbourne atlases (Shirer et al., 2012; Tian et al., 2020).

Supplementary Fig 4. (a) Spatial reproducibility (Dice similarity coefficient) of the thresholded static functional connectivity (FC) t-maps between the VU 3T-ME, HCP 3T, and HCP 7T datasets for each preprocessing pipeline (mCSF/WM, physio, and aCompCor). (b) Spatial reproducibility (Dice similarity coefficient) of the thresholded static FC t-maps between the mCSF/WM, physio, and aCompCor pipelines for each fMRI dataset.

Supplementary Fig 5. (a, c) Vigilance-dependent functional connectivity (FC) t-maps of the locus coresuleus (LC), cuneiform/subcuneiform nucleus (CSC), and nucleus basalis of Meynert (NBM) in the VU 3T-ME dataset for the physio and aCompCor preprocessing pipelines. The FC t-maps were thresholded at 40% of the top t-values in the gray matter and at $p < 0.05$ (voxel-wise false discovery rate [FDR]-corrected over the entire gray matter volume). AFNI was used for visualization of the t-maps (@chauffeur_afni function; upper functional range set to the 98th percentile). (b, d) Spatial overlap of the thresholded vigilance-dependent FC t-maps of the subcortical arousal regions with 16 canonical brain network templates from the FINDLAB and Melbourne atlases (Shirer et al., 2012; Tian et al., 2020).

Supplementary Fig 6. Spatial reproducibility (Dice similarity coefficient) of the thresholded vigilance-dependent functional connectivity (FC) t-maps between the mCSF/WM, physio, and aCompCor pipelines in the VU 3T-ME dataset.

22

REFERENCES

827

828 Abe, T., 2023. PERCLOS-based technologies for detecting drowsiness: current evidence and
829 future directions. Sleep Adv 4, zpad006.

830 Allen, E.A., Damaraju, E., Plis, S.M., Erhardt, E.B., Eichele, T., Calhoun, V.D., 2014. Tracking
831 whole-brain connectivity dynamics in the resting state. Cereb Cortex 24, 663-676.

832 Bagshaw, A.P., Hale, J.R., Campos, B.M., Rollings, D.T., Wilson, R.S., Alvim, M.K.M., Coan,
833 A.C., Cendes, F., 2017. Sleep onset uncovers thalamic abnormalities in patients with idiopathic
834 generalised epilepsy. Neuroimage Clin 16, 52-57.

835 Bar, K.J., de la Cruz, F., Schumann, A., Koehler, S., Sauer, H., Critchley, H., Wagner, G., 2016.
836 Functional connectivity and network analysis of midbrain and brainstem nuclei. Neuroimage
837 134, 53-63.

838 Behzadi, Y., Restom, K., Liau, J., Liu, T.T., 2007. A component based noise correction method
839 (CompCor) for BOLD and perfusion based fMRI. Neuroimage 37, 90-101.

840 Beissner, F., 2015. Functional MRI of the Brainstem: Common Problems and their Solutions.
841 Clin Neuroradiol 25 Suppl 2, 251-257.

842 Beliveau, V., Svarer, C., Frokjaer, V.G., Knudsen, G.M., Greve, D.N., Fisher, P.M., 2015.
843 Functional connectivity of the dorsal and median raphe nuclei at rest. Neuroimage 116, 187-
844 195.

845 Benarroch, E.E., 2018. Brainstem integration of arousal, sleep, cardiovascular, and respiratory
846 control. Neurology 91, 958-966.

847 Bernier, M., Cunnane, S.C., Whittingstall, K., 2018. The morphology of the human
848 cerebrovascular system. Hum Brain Mapp 39, 4962-4975.

849 Brooks, J.C., Faull, O.K., Pattinson, K.T., Jenkinson, M., 2013. Physiological noise in brainstem
850 FMRI. Front Hum Neurosci 7, 623.

851 Brown, R.E., Basheer, R., McKenna, J.T., Strecker, R.E., McCarley, R.W., 2012. Control of
852 sleep and wakefulness. Physiol Rev 92, 1087-1187.

853 Buckner, R.L., DiNicola, L.M., 2019. The brain's default network: updated anatomy, physiology
854 and evolving insights. Nat Rev Neurosci 20, 593-608.

855 Caballero-Gaudes, C., Reynolds, R.C., 2017. Methods for cleaning the BOLD fMRI signal.
856 Neuroimage 154, 128-149.

857 Canales-Johnson, A., Beerendonk, L., Blain, S., Kitaoka, S., Ezquerro-Nassar, A., Nuiten, S.,
858 Fahrenfort, J., van Gaal, S., Bekinschtein, T.A., 2020. Decreased Alertness Reconfigures
859 Cognitive Control Networks. J Neurosci 40, 7142-7154.

860 Cauzzo, S., Singh, K., Stauder, M., Garcia-Gomar, M.G., Vanello, N., Passino, C., Staab, J.,
861 Indovina, I., Bianciardi, M., 2022. Functional connectome of brainstem nuclei involved in

862   autonomic, limbic, pain and sensory processing in living humans from 7 Tesla resting state
863   fMRI. Neuroimage 250, 118925.

864   Chang, C., Cunningham, J.P., Glover, G.H., 2009. Influence of heart rate on the BOLD signal:
865   the cardiac response function. Neuroimage 44, 857-869.

866   Chang, C., Liu, Z., Chen, M.C., Liu, X., Duyn, J.H., 2013. EEG correlates of time-varying BOLD
867   functional connectivity. Neuroimage 72, 227-236.

868   Chang, C., Raven, E.P., Duyn, J.H., 2016. Brain-heart interactions: challenges and
869   opportunities with functional magnetic resonance imaging at ultra-high field. Philos Trans A
870   Math Phys Eng Sci 374.

871   Chen, G., Saad, Z.S., Britton, J.C., Pine, D.S., Cox, R.W., 2013. Linear mixed-effects modeling
872   approach to FMRI group analysis. Neuroimage 73, 176-190.

873   Chen, J.E., Lewis, L.D., Chang, C., Tian, Q., Fultz, N.E., Ohringer, N.A., Rosen, B.R., Polimeni,
874   J.R., 2020. Resting-state "physiological networks". Neuroimage 213, 116707.

875   Ding, F., O'Donnell, J., Xu, Q., Kang, N., Goldman, N., Nedergaard, M., 2016. Changes in the
876   composition of brain interstitial ions control the sleep-wake cycle. Science 352, 550-555.

877   Doss, D.J., Johnson, G.W., Narasimhan, S., Shless, J.S., Jiang, J.W., Gonzalez, H.F.J., Paulo,
878   D.L., Lucas, A., Davis, K.A., Chang, C., Morgan, V.L., Constantinidis, C., Dawant, B.M., Englot,
879   D.J., 2023. Deep Learning Segmentation of the Nucleus Basalis of Meynert on 3T MRI. AJNR
880   Am J Neuroradiol 44, 1020-1025.

881   Edlow, B.L., Claassen, J., Schiff, N.D., Greer, D.M., 2021. Recovery from disorders of
882   consciousness: mechanisms, prognosis and emerging therapies. Nat Rev Neurol 17, 135-156.

883   Edlow, B.L., Olchanyi, M., Freeman, H.J., Li, J., Maffei, C., Snider, S.B., Zollei, L., Iglesias, J.E.,
884   Augustinack, J., Bodien, Y.G., Haynes, R.L., Greve, D.N., Diamond, B.R., Stevens, A., Giacino,
885   J.T., Destrieux, C., van der Kouwe, A., Brown, E.N., Folkerth, R.D., Fischl, B., Kinney, H.C.,
886   2024. Multimodal MRI reveals brainstem connections that sustain wakefulness in human
887   consciousness. Sci Transl Med 16, eadj4303.

888   Edlow, B.L., Takahashi, E., Wu, O., Benner, T., Dai, G., Bu, L., Grant, P.E., Greer, D.M.,
889   Greenberg, S.M., Kinney, H.C., Folkerth, R.D., 2012. Neuroanatomic connectivity of the human
890   ascending arousal system critical to consciousness and its disorders. J Neuropathol Exp Neurol
891   71, 531-546.

892   Engelen, T., Solca, M., Tallon-Baudry, C., 2023. Interoceptive rhythms in the brain. Nat
893   Neurosci 26, 1670-1684.

894   Englot, D.J., Gonzalez, H.F.J., Reynolds, B.B., Konrad, P.E., Jacobs, M.L., Gore, J.C.,
895   Landman, B.A., Morgan, V.L., 2018. Relating structural and functional brainstem connectivity to
896   disease measures in epilepsy. Neurology 91, e67-e77.

897   Englot, D.J., Morgan, V.L., Chang, C., 2020. Impaired vigilance networks in temporal lobe
898   epilepsy: Mechanisms and clinical implications. Epilepsia 61, 189-202.

899   Falahpour, M., Chang, C., Wong, C.W., Liu, T.T., 2018. Template-based prediction of vigilance
900   fluctuations in resting-state fMRI. Neuroimage 174, 317-327.

901   Franzen, P.L., Siegle, G.J., Buysse, D.J., 2008. Relationships between affect, vigilance, and
902   sleepiness following sleep deprivation. J Sleep Res 17, 34-41.

903   Fultz, N.E., Bonmassar, G., Setsompop, K., Stickgold, R.A., Rosen, B.R., Polimeni, J.R., Lewis,
904   L.D., 2019. Coupled electrophysiological, hemodynamic, and cerebrospinal fluid oscillations in
905   human sleep. Science 366, 628-631.

906   Gold, B.P., Goodale, S.E., Zhao, C., Pourmotabbed, H., de Zwart, J.A., Özbay, P.S., Bolt, T.S.,
907   Duyn, J.H., Chen, J.E., Chang, C., 2024. Functional MRI signals exhibit stronger covariation
908   with peripheral autonomic measures as vigilance decreases. Imaging Neuroscience 2, 1-25.

909   Gonzalez-Castillo, J., Fernandez, I.S., Handwerker, D.A., Bandettini, P.A., 2022. Ultra-slow
910   fMRI fluctuations in the fourth ventricle as a marker of drowsiness. Neuroimage 259, 119424.

911   Gonzalez, H.F.J., Narasimhan, S., Goodale, S.E., Johnson, G.W., Doss, D.J., Paulo, D.L.,
912   Morgan, V.L., Chang, C., Englot, D.J., 2023. Arousal and salience network connectivity
913   alterations in surgical temporal lobe epilepsy. J Neurosurg 138, 810-820.

914   Gonzalez, H.F.J., Narasimhan, S., Johnson, G.W., Wills, K.E., Haas, K.F., Konrad, P.E., Chang,
915   C., Morgan, V.L., Rubinov, M., Englot, D.J., 2021. Role of the Nucleus Basalis as a Key
916   Network Node in Temporal Lobe Epilepsy. Neurology 96, e1334-e1346.

917   Goodale, S.E., Ahmed, N., Zhao, C., de Zwart, J.A., Ozbay, P.S., Picchioni, D., Duyn, J., Englot,
918   D.J., Morgan, V.L., Chang, C., 2021. fMRI-based detection of alertness predicts behavioral
919   response variability. Elife 10.

920   Grimm, C., Duss, S.N., Privitera, M., Munn, B.R., Karalis, N., Frassle, S., Wilhelm, M.,
921   Patriarchi, T., Razansky, D., Wenderoth, N., Shine, J.M., Bohacek, J., Zerbi, V., 2024. Tonic
922   and burst-like locus coeruleus stimulation distinctly shift network activity across the cortical
923   hierarchy. Nat Neurosci.

924   Grothe, M.J., Schuster, C., Bauer, F., Heinsen, H., Prudlo, J., Teipel, S.J., 2014. Atrophy of the
925   cholinergic basal forebrain in dementia with Lewy bodies and Alzheimer's disease dementia. J
926   Neurol 261, 1939-1948.

927   Gu, Y., Han, F., Sainburg, L.E., Schade, M.M., Buxton, O.M., Duyn, J.H., Liu, X., 2022. An
928   orderly sequence of autonomic and neural events at transient arousal changes. Neuroimage
929   264, 119720.

930   Gu, Y., Sainburg, L.E., Kuang, S., Han, F., Williams, J.W., Liu, Y., Zhang, N., Zhang, X.,
931   Leopold, D.A., Liu, X., 2021. Brain Activity Fluctuations Propagate as Waves Traversing the
932   Cortical Hierarchy. Cereb Cortex 31, 3986-4005.

933   Guardia, T., Geerligs, L., Tsvetanov, K.A., Ye, R., Campbell, K.L., 2022. The role of the arousal
934   system in age-related differences in cortical functional network architecture. Hum Brain Mapp
935   43, 985-997.

936 Guo, Y., Chen, Y., Shao, Y., Hu, S., Zou, G., Chen, J., Li, Y., Gao, X., Liu, J., Yao, P., Zhou, S.,
937 Xu, J., Gao, J.H., Zou, Q., Sun, H., 2023. Thalamic network under wakefulness after sleep
938 onset and its coupling with daytime fatigue in insomnia disorder: An EEG-fMRI study. J Affect
939 Disord 334, 92-99.

940 Hansen, J.Y., Cauzzo, S., Singh, K., Garcia-Gomar, M.G., Shine, J.M., Bianciardi, M., Misic, B.,
941 2024. Integrating brainstem and cortical functional architectures. Nat Neurosci.

942 Harrison, B.J., Davey, C.G., Savage, H.S., Jamieson, A.J., Leonards, C.A., Moffat, B.A., Glarin,
943 R.K., Steward, T., 2022. Dynamic subcortical modulators of human default mode network
944 function. Cereb Cortex 32, 4345-4355.

945 Hegerl, U., Hensch, T., 2014. The vigilance regulation model of affective disorders and ADHD.
946 Neurosci Biobehav Rev 44, 45-57.

947 Helakari, H., Korhonen, V., Holst, S.C., Piispala, J., Kallio, M., Vayrynen, T., Huotari, N.,
948 Raitamaa, L., Tuunanen, J., Kananen, J., Jarvela, M., Tuovinen, T., Raatikainen, V., Borchardt,
949 V., Kinnunen, H., Nedergaard, M., Kiviniemi, V., 2022. Human NREM Sleep Promotes Brain-
950 Wide Vasomotor and Respiratory Pulsations. J Neurosci 42, 2503-2515.

951 Helwegen, K., Libedinsky, I., van den Heuvel, M.P., 2023. Statistical power in network
952 neuroscience. Trends Cogn Sci 27, 282-301.

953 Herrero, J.L., Khuvis, S., Yeagle, E., Cerf, M., Mehta, A.D., 2018. Breathing above the brain
954 stem: volitional control and attentional modulation in humans. J Neurophysiol 119, 145-159.

955 Huang, J., Sander, C., Jawinski, P., Ulke, C., Spada, J., Hegerl, U., Hensch, T., 2015. Test-
956 retest reliability of brain arousal regulation as assessed with VIGALL 2.0. Neuropsychiatric
957 Electrophysiology 1, 13.

958 Iacovella, V., Hasson, U., 2011. The relationship between BOLD signal and autonomic nervous
959 system functions: implications for processing of "physiological noise". Magn Reson Imaging 29,
960 1338-1345.

961 Jagannathan, S.R., Bareham, C.A., Bekinschtein, T.A., 2022. Decreasing Alertness Modulates
962 Perceptual Decision-Making. J Neurosci 42, 454-473.

963 Jawinski, P., Kirsten, H., Sander, C., Spada, J., Ulke, C., Huang, J., Burkhardt, R., Scholz, M.,
964 Hensch, T., Hegerl, U., 2019. Human brain arousal in the resting state: a genome-wide
965 association study. Mol Psychiatry 24, 1599-1609.

966 Joshi, S., 2021. Pupillometry: Arousal State or State of Mind? Curr Biol 31, R32-R34.

967 Joshi, S., Li, Y., Kalwani, R.M., Gold, J.I., 2016. Relationships between Pupil Diameter and
968 Neuronal Activity in the Locus Coeruleus, Colliculi, and Cingulate Cortex. Neuron 89, 221-234.

969 Kelberman, M., Keilholz, S., Weinshenker, D., 2020. What's That (Blue) Spot on my MRI?
970 Multimodal Neuroimaging of the Locus Coeruleus in Neurodegenerative Disease. Front
971 Neurosci 14, 583421.

972   Kelly, C., de Zubicaray, G., Di Martino, A., Copland, D.A., Reiss, P.T., Klein, D.F., Castellanos,
973   F.X., Milham, M.P., McMahon, K., 2009. L-dopa modulates functional connectivity in striatal
974   cognitive and motor networks: a double-blind placebo-controlled study. J Neurosci 29, 7364-
975   7378.

976   Kluger, D.S., Gross, J., 2021. Respiration modulates oscillatory neural network activity at rest.
977   PLoS Biol 19, e3001457.

978   Kundu, P., Brenowitz, N.D., Voon, V., Worbe, Y., Vertes, P.E., Inati, S.J., Saad, Z.S., Bandettini,
979   P.A., Bullmore, E.T., 2013. Integrated strategy for improving functional connectivity mapping
980   using multiecho fMRI. Proc Natl Acad Sci U S A 110, 16187-16192.

981   Kundu, P., Inati, S.J., Evans, J.W., Luh, W.M., Bandettini, P.A., 2012. Differentiating BOLD and
982   non-BOLD signals in fMRI time series using multi-echo EPI. Neuroimage 60, 1759-1770.

983   Larsen, R.S., Waters, J., 2018. Neuromodulatory Correlates of Pupil Dilation. Front Neural
984   Circuits 12, 21.

985   Lewis, L.D., 2021. The interconnected causes and consequences of sleep in the brain. Science
986   374, 564-568.

987   Li, A., Liu, H., Lei, X., He, Y., Wu, Q., Yan, Y., Zhou, X., Tian, X., Peng, Y., Huang, S., Li, K.,
988   Wang, M., Sun, Y., Yan, H., Zhang, C., He, S., Han, R., Wang, X., Liu, B., 2023. Hierarchical
989   fluctuation shapes a dynamic flow linked to states of consciousness. Nat Commun 14, 3238.

990   Li, C.S., Ide, J.S., Zhang, S., Hu, S., Chao, H.H., Zaborszky, L., 2014. Resting state functional
991   connectivity of the basal nucleus of Meynert in humans: in comparison to the ventral striatum
992   and the effects of age. Neuroimage 97, 321-332.

993   Liu, T.T., 2016. Noise contributions to the fMRI signal: An overview. Neuroimage 143, 141-151.

994   Liu, T.T., Falahpour, M., 2020. Vigilance Effects in Resting-State fMRI. Front Neurosci 14, 321.

995   Liu, T.T., Nalci, A., Falahpour, M., 2017. The global signal in fMRI: Nuisance or Information?
996   Neuroimage 150, 213-229.

997   Liu, X., de Zwart, J.A., Scholvinck, M.L., Chang, C., Ye, F.Q., Leopold, D.A., Duyn, J.H., 2018.
998   Subcortical evidence for a contribution of arousal to fMRI studies of brain activity. Nat Commun
999   9, 395.

1000   Liu, X., Yanagawa, T., Leopold, D.A., Chang, C., Ishida, H., Fujii, N., Duyn, J.H., 2015. Arousal
1001   transitions in sleep, wakefulness, and anesthesia are characterized by an orderly sequence of
1002   cortical events. Neuroimage 116, 222-231.

1003   Lorincz, M.L., Adamantidis, A.R., 2017. Monoaminergic control of brain states and sensory
1004   processing: Existing knowledge and recent insights obtained with optogenetics. Prog Neurobiol
1005   151, 237-253.

1006   Maki-Marttunen, V., Espeseth, T., 2021. Uncovering the locus coeruleus: Comparison of
1007   localization methods for functional analysis. Neuroimage 224, 117409.

1008 Martin, C.G., He, B.J., Chang, C., 2021. State-related neural influences on fMRI connectivity
1009 estimation. Neuroimage 244, 118590.

1010 Mather, M., Clewett, D., Sakaki, M., Harley, C.W., 2016. Norepinephrine ignites local hotspots of
1011 neuronal excitation: How arousal amplifies selectivity in perception and memory. Behav Brain
1012 Sci 39, e200.

1013 Mieling, M., Gottlich, M., Yousuf, M., Bunzeck, N., 2023. Basal forebrain activity predicts
1014 functional degeneration in the entorhinal cortex in Alzheimer's disease. Brain Commun 5,
1015 fcad262.

1016 Murphy, K., Fox, M.D., 2017. Towards a consensus regarding global signal regression for
1017 resting state functional connectivity MRI. Neuroimage 154, 169-173.

1018 Murphy, P.R., O'Connell, R.G., O'Sullivan, M., Robertson, I.H., Balsters, J.H., 2014. Pupil
1019 diameter covaries with BOLD activity in human locus coeruleus. Hum Brain Mapp 35, 4140-
1020 4154.

1021 Nair, J., Klaassen, A.L., Arato, J., Vyssotski, A.L., Harvey, M., Rainer, G., 2018. Basal forebrain
1022 contributes to default mode network regulation. Proc Natl Acad Sci U S A 115, 1352-1357.

1023 Nalci, A., Rao, B.D., Liu, T.T., 2017. Global signal regression acts as a temporal downweighting
1024 process in resting-state fMRI. Neuroimage 152, 602-618.

1025 Oken, B.S., Salinsky, M.C., Elsas, S.M., 2006. Vigilance, alertness, or sustained attention:
1026 physiological basis and measurement. Clin Neurophysiol 117, 1885-1901.

1027 Olbrich, S., Mulert, C., Karch, S., Trenner, M., Leicht, G., Pogarell, O., Hegerl, U., 2009. EEG-
1028 vigilance and BOLD effect during simultaneous EEG/fMRI measurement. Neuroimage 45, 319-
1029 332.

1030 Ong, J.L., Kong, D., Chia, T.T., Tandi, J., Thomas Yeo, B.T., Chee, M.W., 2015. Co-activated
1031 yet disconnected-Neural correlates of eye closures when trying to stay awake. Neuroimage 118,
1032 553-562.

1033 Oyarzabal, E.A., Hsu, L.M., Das, M., Chao, T.H., Zhou, J., Song, S., Zhang, W., Smith, K.G.,
1034 Sciolino, N.R., Evsyukova, I.Y., Yuan, H., Lee, S.H., Cui, G., Jensen, P., Shih, Y.I., 2022.
1035 Chemogenetic stimulation of tonic locus coeruleus activity strengthens the default mode
1036 network. Sci Adv 8, eabm9898.

1037 Ozbay, P.S., Chang, C., Picchioni, D., Mandelkow, H., Chappel-Farley, M.G., van Gelderen, P.,
1038 de Zwart, J.A., Duyn, J., 2019. Sympathetic activity contributes to the fMRI signal. Commun Biol
1039 2, 421.

1040 Perslev, M., Darkner, S., Kempfner, L., Nikolic, M., Jennum, P.J., Igel, C., 2021. U-Sleep:
1041 resilient high-frequency sleep staging. NPJ Digit Med 4, 72.

1042 Picchioni, D., Ozbay, P.S., Mandelkow, H., de Zwart, J.A., Wang, Y., van Gelderen, P., Duyn,
1043 J.H., 2022. Autonomic arousals contribute to brain fluid pulsations during sleep. Neuroimage
1044 249, 118888.

Poe, G.R., Foote, S., Eschenko, O., Johansen, J.P., Bouret, S., Aston-Jones, G., Harley, C.W., Manahan-Vaughan, D., Weinshenker, D., Valentino, R., Berridge, C., Chandler, D.J., Waterhouse, B., Sara, S.J., 2020. Locus coeruleus: a new look at the blue spot. Nat Rev Neurosci 21, 644-659.

Pourmotabbed, H., Vivek, A., Martin, C., Goodale, S., Wang, S., Morgan, V., Englot, D., Chang, C., 2024. Low-dimensional representation of fMRI disentangles temporal contributions of EEG-determined vigilance from other global effects. SPIE Medical Imaging. SPIE.

Power, J.D., Lynch, C.J., Dubin, M.J., Silver, B.M., Martin, A., Jones, R.M., 2020. Characteristics of respiratory measures in young adults scanned at rest, including systematic changes and "missed" deep breaths. Neuroimage 204, 116234.

Rasmussen, R., O'Donnell, J., Ding, F., Nedergaard, M., 2020. Interstitial ions: A key regulator of state-dependent neural activity? Prog Neurobiol 193, 101802.

Raut, R.V., Snyder, A.Z., Mitra, A., Yellin, D., Fujii, N., Malach, R., Raichle, M.E., 2021. Global waves synchronize the brain's functional systems with fluctuating arousal. Sci Adv 7.

Ray, N.J., Bradburn, S., Murgatroyd, C., Toseeb, U., Mir, P., Kountouriotis, G.K., Teipel, S.J., Grothe, M.J., 2018. In vivo cholinergic basal forebrain atrophy predicts cognitive decline in de novo Parkinson's disease. Brain 141, 165-176.

Rothman, S.M., Mattson, M.P., 2012. Sleep disturbances in Alzheimer's and Parkinson's diseases. Neuromolecular Med 14, 194-204.

Samann, P.G., Wehrle, R., Hoehn, D., Spoormaker, V.I., Peters, H., Tully, C., Holsboer, F., Czisch, M., 2011. Development of the brain's default mode network from wakefulness to slow wave sleep. Cereb Cortex 21, 2082-2093.

Sander, C., Hensch, T., Wittekind, D.A., Bottger, D., Hegerl, U., 2015. Assessment of Wakefulness and Brain Arousal Regulation in Psychiatric Research. Neuropsychobiology 72, 195-205.

Sandsmark, D.K., Elliott, J.E., Lim, M.M., 2017. Sleep-Wake Disturbances After Traumatic Brain Injury: Synthesis of Human and Animal Studies. Sleep 40.

Sara, S.J., Bouret, S., 2012. Orienting and reorienting: the locus coeruleus mediates cognition through arousal. Neuron 76, 130-141.

Scammell, T.E., Arrigoni, E., Lipton, J.O., 2017. Neural Circuitry of Wakefulness and Sleep. Neuron 93, 747-765.

Schaefer, A., Kong, R., Gordon, E.M., Laumann, T.O., Zuo, X.N., Holmes, A.J., Eickhoff, S.B., Yeo, B.T.T., 2018. Local-Global Parcellation of the Human Cerebral Cortex from Intrinsic Functional Connectivity MRI. Cereb Cortex 28, 3095-3114.

Schmitz, T.W., Nathan Spreng, R., Alzheimer's Disease Neuroimaging, I., 2016. Basal forebrain degeneration precedes and predicts the cortical spread of Alzheimer's pathology. Nat Commun 7, 13249.

1082 Schneider, M., Hathway, P., Leuchs, L., Samann, P.G., Czisch, M., Spoormaker, V.I., 2016.
1083 Spontaneous pupil dilations during the resting state are associated with activation of the
1084 salience network. Neuroimage 139, 189-201.

1085 Sclocco, R., Beissner, F., Bianciardi, M., Polimeni, J.R., Napadow, V., 2018. Challenges and
1086 opportunities for brainstem neuroimaging with ultrahigh field MRI. Neuroimage 168, 412-426.

1087 Seidel, K., Mahlke, J., Siswanto, S., Kruger, R., Heinsen, H., Auburger, G., Bouzrou, M.,
1088 Grinberg, L.T., Wicht, H., Korf, H.W., den Dunnen, W., Rub, U., 2015. The brainstem
1089 pathologies of Parkinson's disease and dementia with Lewy bodies. Brain Pathol 25, 121-135.

1090 Serra, L., D'Amelio, M., Di Domenico, C., Dipasquale, O., Marra, C., Mercuri, N.B., Caltagirone,
1091 C., Cercignani, M., Bozzali, M., 2018. In vivo mapping of brainstem nuclei functional connectivity
1092 disruption in Alzheimer's disease. Neurobiol Aging 72, 72-82.

1093 Shekari Soleimanloo, S., Wilkinson, V.E., Cori, J.M., Westlake, J., Stevens, B., Downey, L.A.,
1094 Shiferaw, B.A., Rajaratnam, S.M.W., Howard, M.E., 2019. Eye-Blink Parameters Detect On-
1095 Road Track-Driving Impairment Following Severe Sleep Deprivation. J Clin Sleep Med 15,
1096 1271-1284.

1097 Shirer, W.R., Ryali, S., Rykhlevskaia, E., Menon, V., Greicius, M.D., 2012. Decoding subject-
1098 driven cognitive states with whole-brain connectivity patterns. Cereb Cortex 22, 158-165.

1099 Smith, S.M., Beckmann, C.F., Andersson, J., Auerbach, E.J., Bijsterbosch, J., Douaud, G., Duff,
1100 E., Feinberg, D.A., Griffanti, L., Harms, M.P., Kelly, M., Laumann, T., Miller, K.L., Moeller, S.,
1101 Petersen, S., Power, J., Salimi-Khorshidi, G., Snyder, A.Z., Vu, A.T., Woolrich, M.W., Xu, J.,
1102 Yacoub, E., Ugurbil, K., Van Essen, D.C., Glasser, M.F., Consortium, W.U.-M.H., 2013.
1103 Resting-state fMRI in the Human Connectome Project. Neuroimage 80, 144-168.

1104 Snider, S.B., Hsu, J., Darby, R.R., Cooke, D., Fischer, D., Cohen, A.L., Grafman, J.H., Fox,
1105 M.D., 2020. Cortical lesions causing loss of consciousness are anticorrelated with the dorsal
1106 brainstem. Hum Brain Mapp 41, 1520-1531.

1107 Soon, C.S., Vinogradova, K., Ong, J.L., Calhoun, V.D., Liu, T., Zhou, J.H., Ng, K.K., Chee,
1108 M.W.L., 2021. Respiratory, cardiac, EEG, BOLD signals and functional connectivity over
1109 multiple microsleep episodes. Neuroimage 237, 118129.

1110 Spindler, L.R.B., Luppi, A.I., Adapa, R.M., Craig, M.M., Coppola, P., Peattie, A.R.D., Manktelow,
1111 A.E., Finoia, P., Sahakian, B.J., Williams, G.B., Allanson, J., Pickard, J.D., Menon, D.K.,
1112 Stamatakis, E.A., 2021. Dopaminergic brainstem disconnection is common to pharmacological
1113 and pathological consciousness perturbation. Proc Natl Acad Sci U S A 118.

1114 Taha, A.A., Hanbury, A., 2015. Metrics for evaluating 3D medical image segmentation: analysis,
1115 selection, and tool. BMC Med Imaging 15, 29.

1116 Taylor, N.L., D'Souza, A., Munn, B.R., Lv, J., Zaborszky, L., Muller, E.J., Wainstein, G.,
1117 Calamante, F., Shine, J.M., 2022. Structural connections between the noradrenergic and
1118 cholinergic system shape the dynamics of functional brain networks. Neuroimage 260, 119455.

1119 Tian, Y., Margulies, D.S., Breakspear, M., Zalesky, A., 2020. Topographic organization of the
1120 human subcortex unveiled with functional connectivity gradients. Nat Neurosci 23, 1421-1432.

1121 Turchi, J., Chang, C., Ye, F.Q., Russ, B.E., Yu, D.K., Cortes, C.R., Monosov, I.E., Duyn, J.H.,
1122 Leopold, D.A., 2018. The Basal Forebrain Regulates Global Resting-State fMRI Fluctuations.
1123 Neuron 97, 940-952 e944.

1124 Turker, H.B., Riley, E., Luh, W.M., Colcombe, S.J., Swallow, K.M., 2021. Estimates of locus
1125 coeruleus function with functional magnetic resonance imaging are influenced by localization
1126 approaches and the use of multi-echo data. Neuroimage 236, 118047.

1127 van den Brink, R.L., Pfeffer, T., Donner, T.H., 2019. Brainstem Modulation of Large-Scale
1128 Intrinsic Cortical Activity Correlations. Front Hum Neurosci 13, 340.

1129 van den Brink, R.L., Pfeffer, T., Warren, C.M., Murphy, P.R., Tona, K.D., van der Wee, N.J.,
1130 Giltay, E., van Noorden, M.S., Rombouts, S.A., Donner, T.H., Nieuwenhuis, S., 2016.
1131 Catecholaminergic Neuromodulation Shapes Intrinsic MRI Functional Connectivity in the Human
1132 Brain. J Neurosci 36, 7865-7876.

1133 Van Essen, D.C., Ugurbil, K., Auerbach, E., Barch, D., Behrens, T.E., Bucholz, R., Chang, A.,
1134 Chen, L., Corbetta, M., Curtiss, S.W., Della Penna, S., Feinberg, D., Glasser, M.F., Harel, N.,
1135 Heath, A.C., Larson-Prior, L., Marcus, D., Michalareas, G., Moeller, S., Oostenveld, R.,
1136 Petersen, S.E., Prior, F., Schlaggar, B.L., Smith, S.M., Snyder, A.Z., Xu, J., Yacoub, E.,
1137 Consortium, W.U.-M.H., 2012. The Human Connectome Project: a data acquisition perspective.
1138 Neuroimage 62, 2222-2231.

1139 van Wingen, G.A., Tendolkar, I., Urner, M., van Marle, H.J., Denys, D., Verkes, R.J., Fernandez,
1140 G., 2014. Short-term antidepressant administration reduces default mode and task-positive
1141 network connectivity in healthy individuals during rest. Neuroimage 88, 47-53.

1142 Wang, C., Ong, J.L., Patanaik, A., Zhou, J., Chee, M.W., 2016. Spontaneous eyelid closures
1143 link vigilance fluctuation with fMRI dynamic connectivity states. Proc Natl Acad Sci U S A 113,
1144 9653-9658.

1145 Wang, J., Sun, J., Gao, L., Zhang, D., Chen, L., Wu, T., 2023. Common and unique
1146 dysconnectivity profiles of dorsal and median raphe in Parkinson's disease. Hum Brain Mapp
1147 44, 1070-1078.

1148 Wang, K., Goodale, S., Doss, D., Gupta, D., Gifford, K., Pechman, K., Hohman, T., Englot, D.,
1149 Jefferson, A., Chang, C., 2024. Investigating interactions between subcortical structure, fMRI
1150 vigilance signals, and cognition in healthy and pathological aging. SPIE Medical Imaging. SPIE.

1151 Ward, A.M., McLaren, D.G., Schultz, A.P., Chhatwal, J., Boot, B.P., Hedden, T., Sperling, R.A.,
1152 2013. Daytime sleepiness is associated with decreased default mode network connectivity in
1153 both young and cognitively intact elderly subjects. Sleep 36, 1609-1615.

1154 Wong, C.W., Olafsson, V., Tal, O., Liu, T.T., 2013. The amplitude of the resting-state fMRI
1155 global signal is related to EEG vigilance measures. Neuroimage 83, 983-990.

1156 Woodrow, R.E., Winzeck, S., Luppi, A.I., Kelleher-Unger, I.R., Spindler, L.R.B., Wilson, J.T.L.,
1157 Newcombe, V.F.J., Coles, J.P., Participants, C.-T.M.S., Investigators, Menon, D.K., Stamatakis,
1158 E.A., 2023. Acute thalamic connectivity precedes chronic post-concussive symptoms in mild
1159 traumatic brain injury. Brain 146, 3484-3499.

1160   Xie, M., Huang, Y., Cai, W., Zhang, B., Huang, H., Li, Q., Qin, P., Han, J., 2024. Neurobiological
1161   Underpinnings of Hyperarousal in Depression: A Comprehensive Review. Brain Sci 14.

1162   Xifra-Porxas, A., Kassinopoulos, M., Mitsis, G.D., 2021. Physiological and motion signatures in
1163   static and time-varying functional connectivity and their subject identifiability. Elife 10.

1164   Yellin, D., Berkovich-Ohana, A., Malach, R., 2015. Coupling between pupil fluctuations and
1165   resting-state fMRI uncovers a slow build-up of antagonistic responses in the human cortex.
1166   Neuroimage 106, 414-427.

1167   Yuan, H., Zotev, V., Phillips, R., Bodurka, J., 2013. Correlated slow fluctuations in respiration,
1168   EEG, and BOLD fMRI. Neuroimage 79, 81-93.

1169   Yuan, R., Biswal, B.B., Zaborszky, L., 2019. Functional Subdivisions of Magnocellular Cell
1170   Groups in Human Basal Forebrain: Test-Retest Resting-State Study at Ultra-high Field, and
1171   Meta-analysis. Cereb Cortex 29, 2844-2858.

1172   Zaborszky, L., Hoemke, L., Mohlberg, H., Schleicher, A., Amunts, K., Zilles, K., 2008.
1173   Stereotaxic probabilistic maps of the magnocellular cell groups in human basal forebrain.
1174   Neuroimage 42, 1127-1141.

1175   Zeng, Q., Qiu, T., Li, K., Luo, X., Wang, S., Xu, X., Liu, X., Hong, L., Li, J., Huang, P., Zhang,
1176   M., Alzheimer's Disease Neuroimaging, I., 2022. Increased functional connectivity between
1177   nucleus basalis of Meynert and amygdala in cognitively intact elderly along the Alzheimer's
1178   continuum. Neuroimage Clin 36, 103256.

1179   Zerbi, V., Floriou-Servou, A., Markicevic, M., Vermeiren, Y., Sturman, O., Privitera, M., von
1180   Ziegler, L., Ferrari, K.D., Weber, B., De Deyn, P.P., Wenderoth, N., Bohacek, J., 2019. Rapid
1181   Reconfiguration of the Functional Connectome after Chemogenetic Locus Coeruleus Activation.
1182   Neuron 103, 702-718 e705.

1183   Zhang, S., Hu, S., Chao, H.H., Li, C.S., 2016. Resting-State Functional Connectivity of the
1184   Locus Coeruleus in Humans: In Comparison with the Ventral Tegmental Area/Substantia Nigra
1185   Pars Compacta and the Effects of Age. Cereb Cortex 26, 3413-3427.

1186

(a) Static FC t-maps of the three fMRI datasets
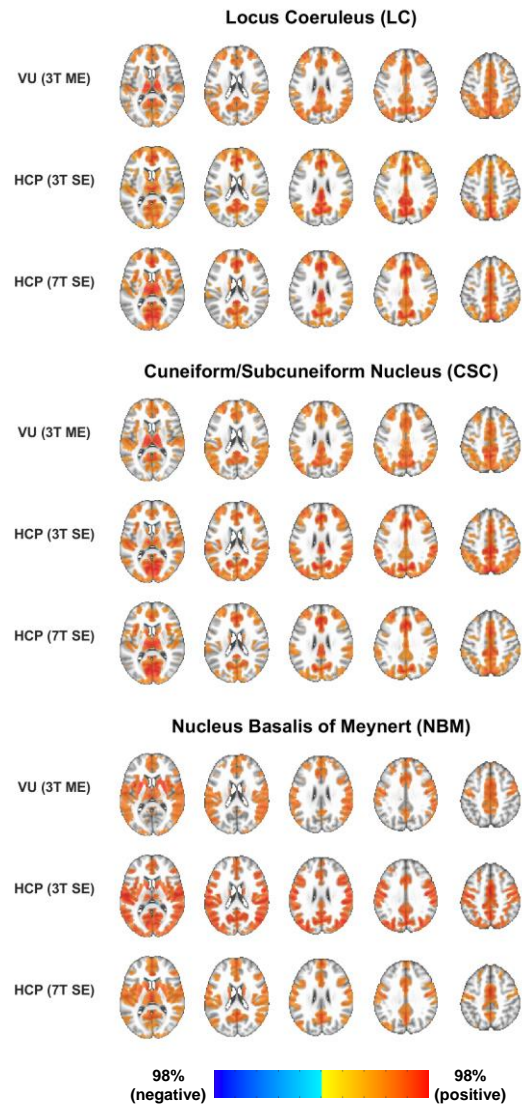
(b) Brain networks in the static FC t-maps
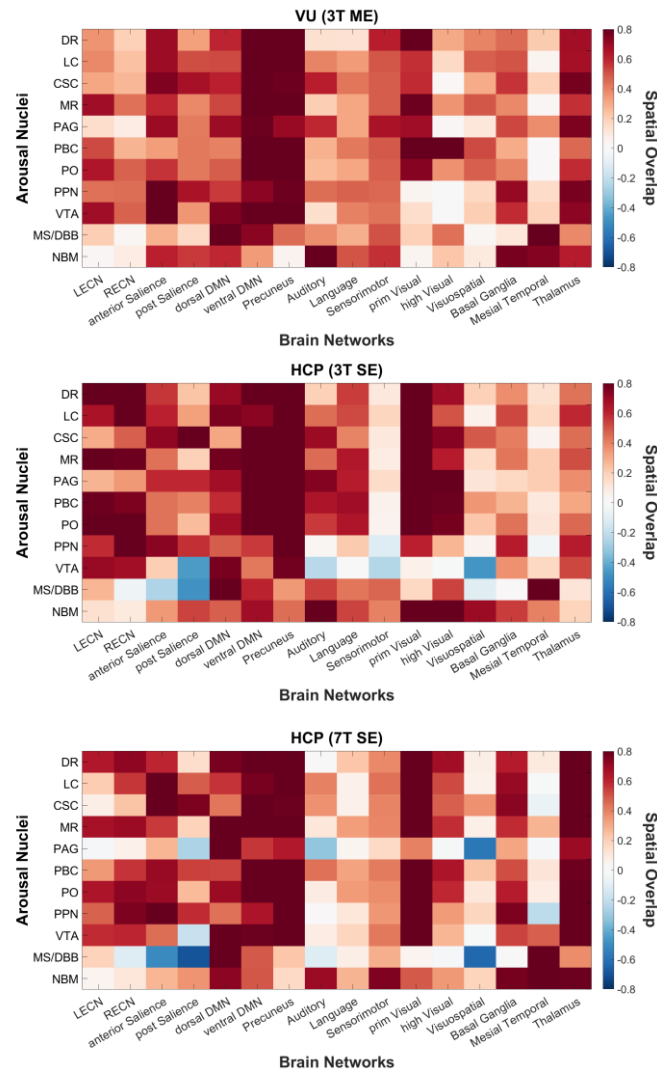
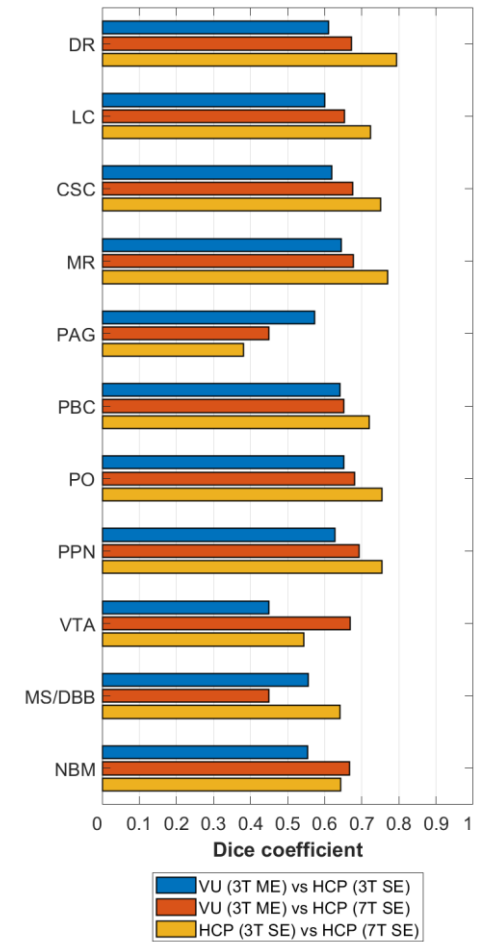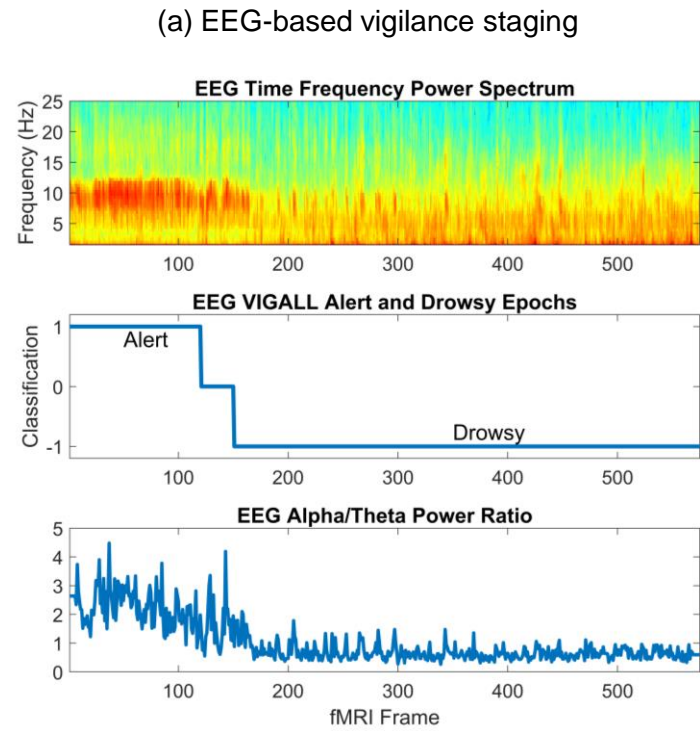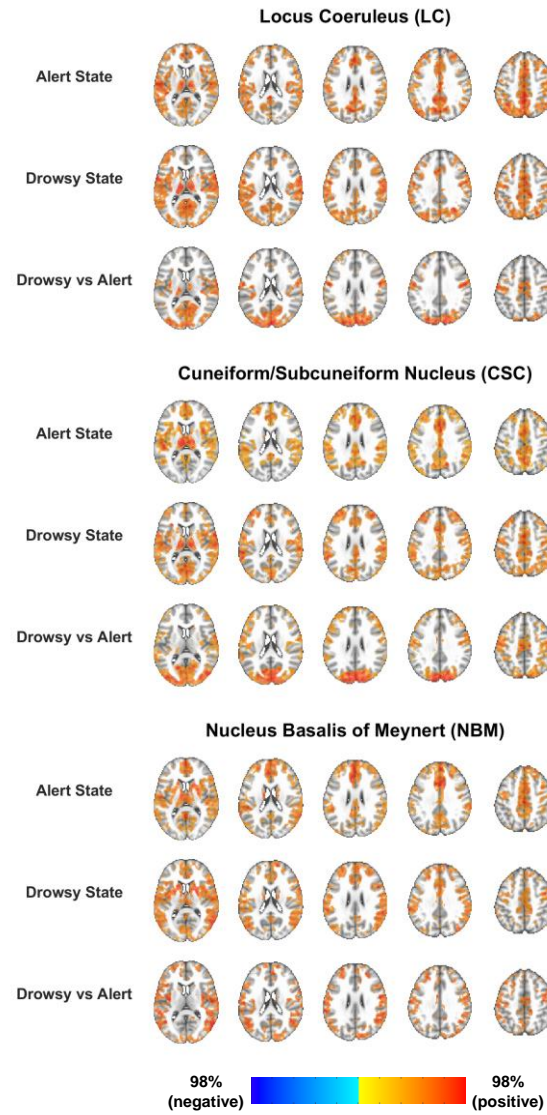(c) Cross-modality reproducibility of the static FC t-maps

Fig. 1.

(a) EEG-based vigilance staging

(b) Vigilance-dependent FC t-maps in the VU 3T-ME dataset
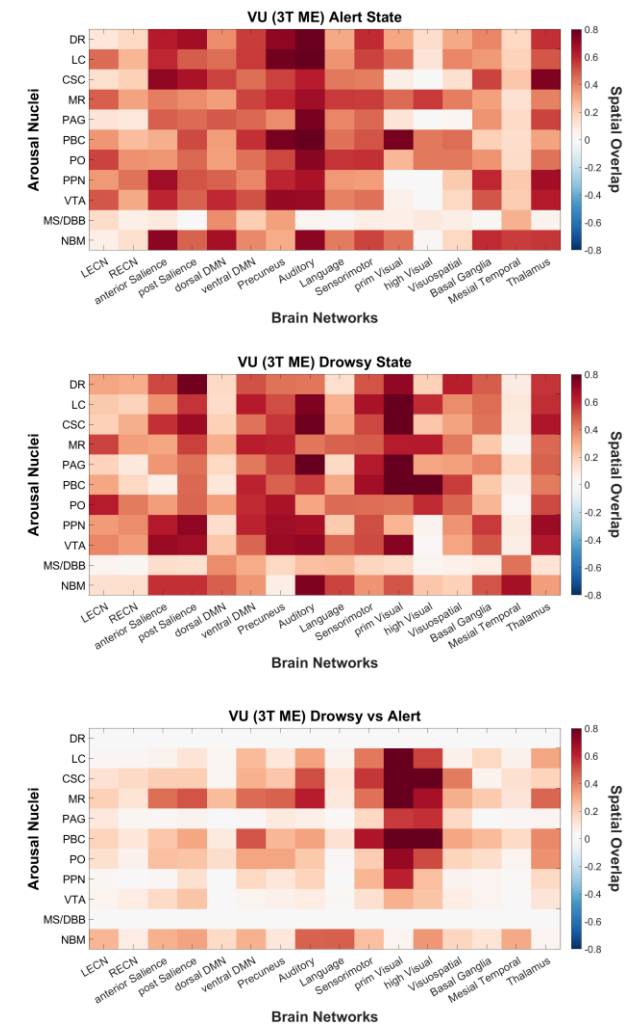
(c) Brain networks in the vigilance-dependent FC t-maps

Fig. 2.

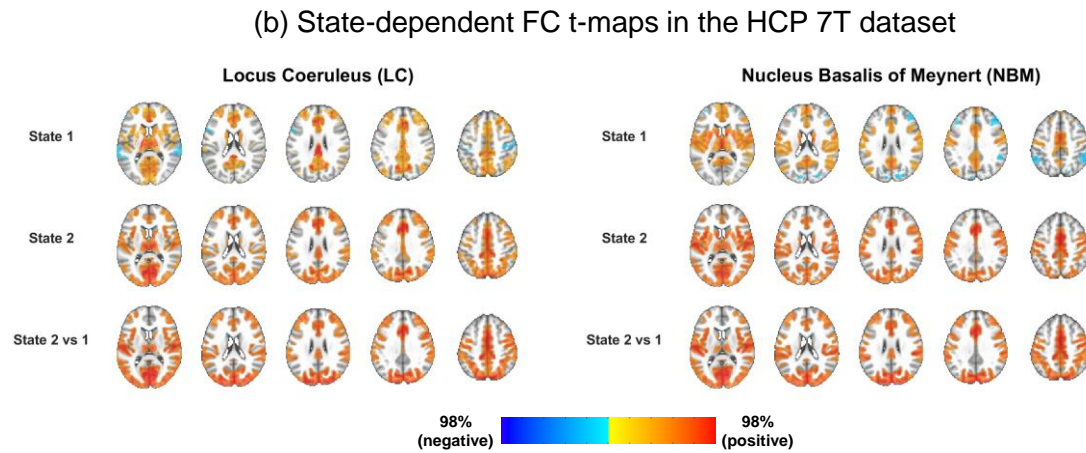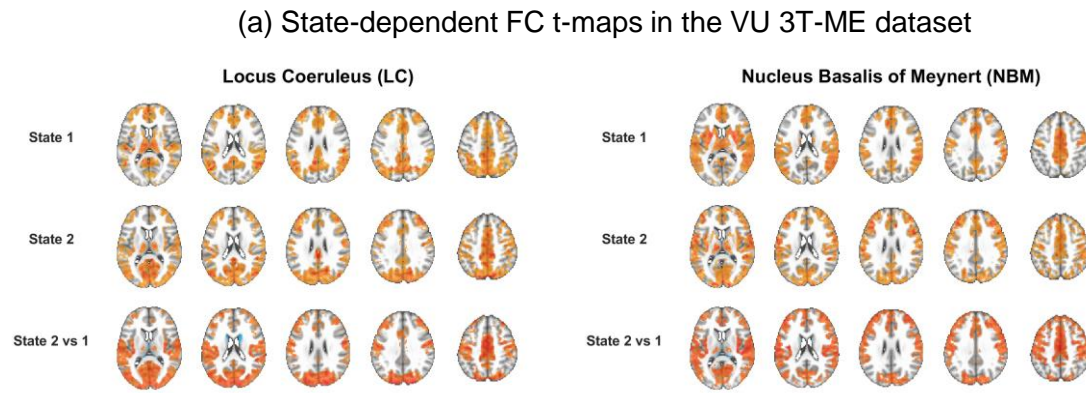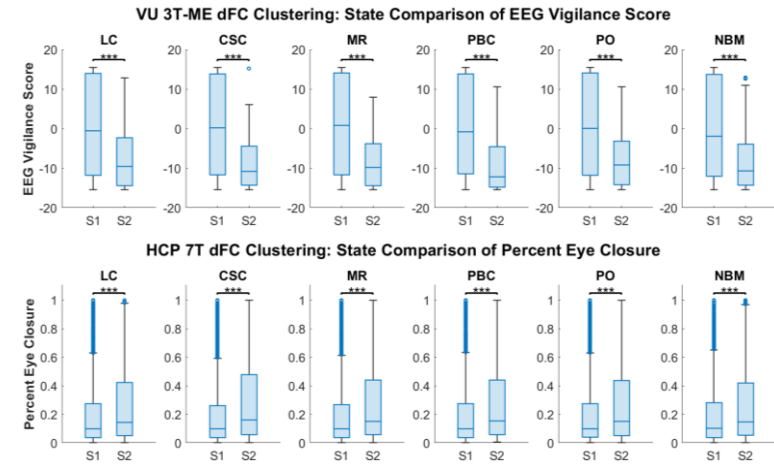(a) State-dependent FC t-maps in the VU 3T-ME dataset

Locus Coeruleus (LC)

Nucleus Basalis of Meynert (NBM)

State 1

State 2

State 2 vs 1

(b) State-dependent FC t-maps in the HCP 7T dataset

Locus Coeruleus (LC)

Nucleus Basalis of Meynert (NBM)

State 1

State 2

State 2 vs 1

98% (negative)   98% (positive)

(c) Comparison of vigilance metrics between the two states

VU 3T-ME dFC Clustering: State Comparison of EEG Vigilance Score

LC   CSC   MR   PBC   PO   NBM

HCP 7T dFC Clustering: State Comparison of Percent Eye Closure

LC   CSC   MR   PBC   PO   NBM

(d) Cross-modality reproducibility of the state-dependent FC t-maps

VU vs HCP 7T state 1   VU vs HCP 7T state 2   VU vs HCP 7T state 2 vs 1

Fig. 3.